NTNU

Norwegian University of
Science and Technology

Modeling burial induced changes in physical sandstone properties

A case-study of North Sea and Norwegian
Sea sandstone formations

Lara Antonia Blazevic
Vucelic

Petroleum Geosciences
Submission date: January 2017
Supervisor: Kenneth Duffaut, IGP
Co-supervisor: Per Åge Avseth, IPT

Norwegian University of Science and Technology
Department of Geoscience and Petroleum

ABSTRACT

The changes in physical properties of sandstones with burial depth are a result of mechanical and chemical compaction processes. These processes are affected by rock microstructure, pressure regimes and temperature history. Data from 30 wells have been used to investigate and compare the changes in porosity, bulk density, elastic moduli and wave propagation velocities between the mid-Jurassic sandstones of the Etive Fm. in the North Sea and the Garn Fm. in the Norwegian Sea.

At shallow burial depths (< 2 km) the changes of the physical properties are governed by effective stress. A mechanical compaction model is used to describe the porosity loss and the bulk density increase with depth, whereas the friable-sand theory is used to explain the changes in elastic moduli and wave propagation velocities. For both formations, the under predictions by the models in the porosity, bulk moduli and P-wave velocity values from the data suggest high depositional porosities (0.40) and small amounts of quartz cement at depths of 1.6-2.0 km.

At greater burial depths and temperatures (> 2 km, > 75°C) quartz cementation is the main controlling factor in the changes of the physical properties. The porosity loss and the bulk density increase with depth are explained by means of a quartz cement precipitation model, and the contact-cement theory is used to describe the changes in elastic moduli and wave propagation velocities. High porosities (> 0.15) at great burial depths (> 4 km) suggest the presence of higher amounts of clay coatings in both formations, and they may also be a result of high overpressures. The great variations in porosity and bulk modulus values for Garn sandstones encountered at same depths, indicate that the Garn Fm. is less well sorted and more affected by different types of quartz deposition than the Etive Fm. The contact-cement model main over prediction trend for the bulk modulus of highly overpressured sandstones enlightens the effects of different pressure regimes in the chemical compaction domain.

ACKNOWLEDGEMENT

Many thanks to Kenneth Duffaut for providing me the data to perform this study, but mostly for his time and dedication as a supervisor. Similarly, I would like to thank my co-supervisor, Per Avseth, for relevant suggestions and discussions during our meetings. Thanks also to Ivan Lehocki for helpful advices regarding the rock physics diagnostics. Thanks to NTNU and to NPD's database for all the relevant resources related to this study.

I am thankful to my family for their support throughout my entire career, for their caring and understanding, and for always being a source of inspiration.

Last but not least, a really heartfelt thank you goes to Stian for his support and company during the writing of this thesis.

TABLE OF CONTENTS

LIST OF FIGURES

CHAPTER 1 INTRODUCTION

The physical properties of rocks are fundamental for the study of sedimentary basins and the characterization of hydrocarbon reservoirs. Properties such as porosity, bulk density and wave propagation velocities of the rock can be obtained or derived from well log data and experimental laboratory measurements, and they may provide information about rock composition and structure.

In a given basin, a sedimentary package deposited at a certain time may present variations in its properties depending on where in the basin is being evaluated, in relation to the depositional environment and the structural evolution of the area. Similarly, the physical properties of a formation change with depth due to compaction. The compaction processes drive the sediments towards higher mechanical and thermodynamic stability (Thyberg and Jahren, 2011). Mechanical compaction starts immediately after deposition and is governed by increasing effective stress, generated from the weight of the overburden, resulting in volume reduction due to rearrangement or breaking of grains (Storvoll et al., 2005, Marcussen et al., 2010, Thyberg and Jahren, 2011). Chemical compaction is controlled by thermodynamics and involves dissolution and precipitation of solids; in clastic sediments, the most important type of chemical compaction is caused by the precipitation of quartz, which begins at 70-80°C (Ehrenberg, 1990, Walderhaug, 1994b).

Storvoll et al. (2005) performed a study where they used well log data from the Norwegian Shelf (North Sea, Norwegian Sea and Barents Sea) to investigate the velocity-depth trends in sedimentary rocks. The authors estimated a linear velocity-depth trend from previously published velocity values, however, the sonic velocity log data showed significant variations from this trend line. For each velocity-depth plot (associated to a specific study area) they separated the data in intervals with different trends, for a better illustration of the variations. The authors concluded that no general velocity-depth function should be used when performing accurate velocity analyses such as depth conversion of seismic data, pore-pressure prediction, or basin modelling.

Marcussen et al. (2010) also performed a study of changes in physical properties with depth for a sandstone Formation in the North Sea (Etive Fm.). The well log data analyzed in their study is compared with experimental mechanical compaction of a sample prepared using sand from the same Etive Fm. The authors noticed that the velocity and density from well log data had an excellent correlation with the results from the experimental mechanical compaction only until certain depths (about 2 km below sea floor). For greater depths, the difference between the experimental results and the well logs show that mechanical compaction alone can no longer explain the depth trends in the Formation (Marcussen et al., 2010). The authors relate the

differences at these depths to the quartz cementation in the sandstone, which is also supported by petrographic analysis of thin section samples. They also concluded that mechanical compaction and quartz cementation are fundamentally different, for which is necessary to model these processes separately when analyzing formations in a basin.

Several compaction trends for different siliciclastic rocks are well documented in the literature. Walderhaug (1996) published a mathematical relationship to model quartz cementation in deep buried sandstones as a function of temperature history. Walderhaug's model also accounts for the effects of grain size, mineralogy, clay coatings and pre-quartz cementation porosity, allowing simulations for different scenarios. For the mechanical compaction domain, Lander and Walderhaug (1999) proposed a model to explain the intergranular volume loss as a function of effective stress.

To study the changes in elastic moduli and velocities as a result of varying rock microstructure, Dvorkin and Nur (1996) presented two theoretical models for high-porosity sandstones. One of the models, the contact-cement model, explained the high velocity values in cemented sandstones, while the second one, the friable-sand model, explained the velocity values for unconsolidated sandstones.

In the present study, the changes in physical properties with burial depth of two time equivalent sandstone formations from the North Sea (Etive Fm.) and the Norwegian Sea (Garn Fm.) are modeled and analyzed with information from 15 wells from each basin. To achieve this, the changes in porosity, bulk density, elastic moduli and wave propagation velocities are studied separately for the mechanical and chemical compaction domains. Combinations of Lander and Walderhaug's model (1999) and the friable-sand model, and of Walderhaug's model (1996) and the contact-cement model are used to describe the changes in these physical properties in the mechanical compaction domain and in the chemical compaction domain, respectively.

The main purpose of this study is to compare the trends of changes in physical properties with burial depth for the Etive Fm. and Garn Fm., and explain their similarities and possible differences. The intention behind this study is also to investigate how different factors related to rock microstructure, pressure regimes and temperature history can affect the mechanical and chemical compaction processes, and how the deviations from the trends can provide further information about these factors.

CHAPTER 2 THEORETICAL BACKGROUND

2.1 Compaction processes

Once sediments are deposited, a series of diagenetic processes start, converting these unconsolidated sediments into sedimentary rocks through physical consolidation and compaction, and chemical processes that involve dissolution and precipitation of minerals (Buller et al., 2005, Bjørlykke and Jahren, 2010). The diagenetic processes change the composition of the sediments and the properties of the rocks, and they are controlled by the temperature history (geothermal gradient), lithostatic stress and pore pressure.

Two main diagenetic processes are mechanical compaction and chemical compaction. Mechanical compaction rearranges the grains to denser packages, resulting in porosity reduction, and is a process governed by the increase of effective stress during burial (Hantschel and Kauerauf, 2009). Chemical compaction involves dissolution of minerals and precipitation of cement, and is controlled by thermodynamics. The precipitation of cement increases the strength of the grain framework and prevents further mechanical compaction (Marcussen et al., 2010). Figure 2.1 illustrates both mechanical and chemical compaction of a grain package after deposition.

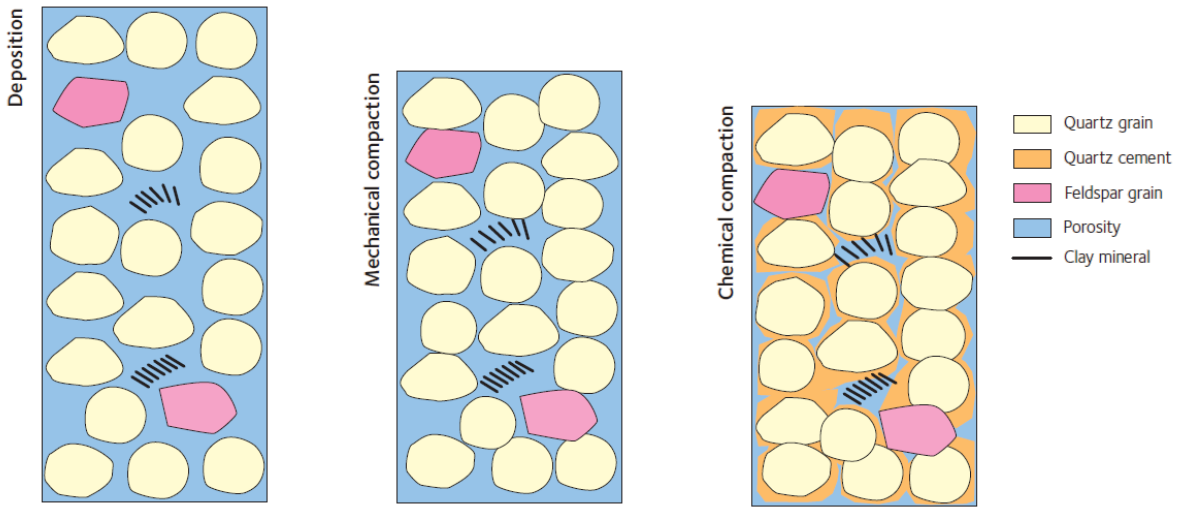

Figure 2.1. Representation of mechanical compaction and chemical compaction after deposition. The initial package configuration (left) is firstly compacted by mechanical forces (center) and subsequently by chemical precipitation of quartz cement (right). (From Buller et al., 2005)

2.1.1 Mechanical compaction

Before quartz cementation, or other types of cementation, grains compact mechanically by sliding and reorientation, and may also fracture due to the overburden stress (Marcussen et al., 2010).

According to Bjørlykke and Jahren (2010), well-sorted sand is generally still loose (if not carbonate cemented) during the first part of its burial history, corresponding to depths of 0-2 km; however, experimental compaction of loose sand with initial porosity of 40-42% shows that the porosity can be reduced to 35-25%, depending on the grain size, at stresses of 20-30 MPa (2-3 km burial for normally pressured rocks) (Chuhan et al., 2002). This confirms that mechanical compaction can have significant effects on porosity, and therefore in the physical properties of the rock, such as elastic moduli, bulk density and wave propagation velocities.

The porosity loss by mechanical compaction determines the intergranular volume (IGV) of the rock at the onset of chemical compaction, which is typically between 25-30% (Marcussen et al., 2010). In some sandstones from the North Sea, Walderhaug (1996) found that the IGV varies from 28-38%.

2.1.2 Chemical compaction

In sedimentary basins with normal geothermal gradients (around 30°C/km), quartz cementation stabilizes the grain framework at about 2 km burial depth (corresponding to 80-100°C), and at greater depths, temperature is the main controlling factor of the compaction, not effective stress (Marcussen et al., 2010). Figure 2.2 shows the transition of mechanical compaction to chemical compaction as a function of stress and depth.

Quartz cementation strengthens the rocks at a faster rate than the increase in overburden stress. According to Bjørlykke and Jahren (2010), in most cases, only 2-4% of quartz cement effectively prevents further mechanical compaction in sandstones, and further compaction is mostly chemically controlled by the rate of mineral dissolution and precipitation.

Once quartz cementation starts and quartz overgrowth is formed, quartz cementation does not cease until most of the porosity disappears (unless the temperatures decrease below 70-80°C). At burial depths of around 4 km (120-140°C), the amount of quartz cement can be 10-15%, and the remaining porosity may be 10-15% (Marcussen et al., 2010).

The amount of quartz cement is primarily a function of the temperature history and the available grain surfaces for quartz precipitation (Walderhaug, 1994b). In 1996, Walderhaug published a mathematical model for quartz cementation prediction, controlled by temperature, time and the grain surface available for quartz precipitation; the most critical parameter for this model is the clay coating, since it determines the area available for quartz cementation.

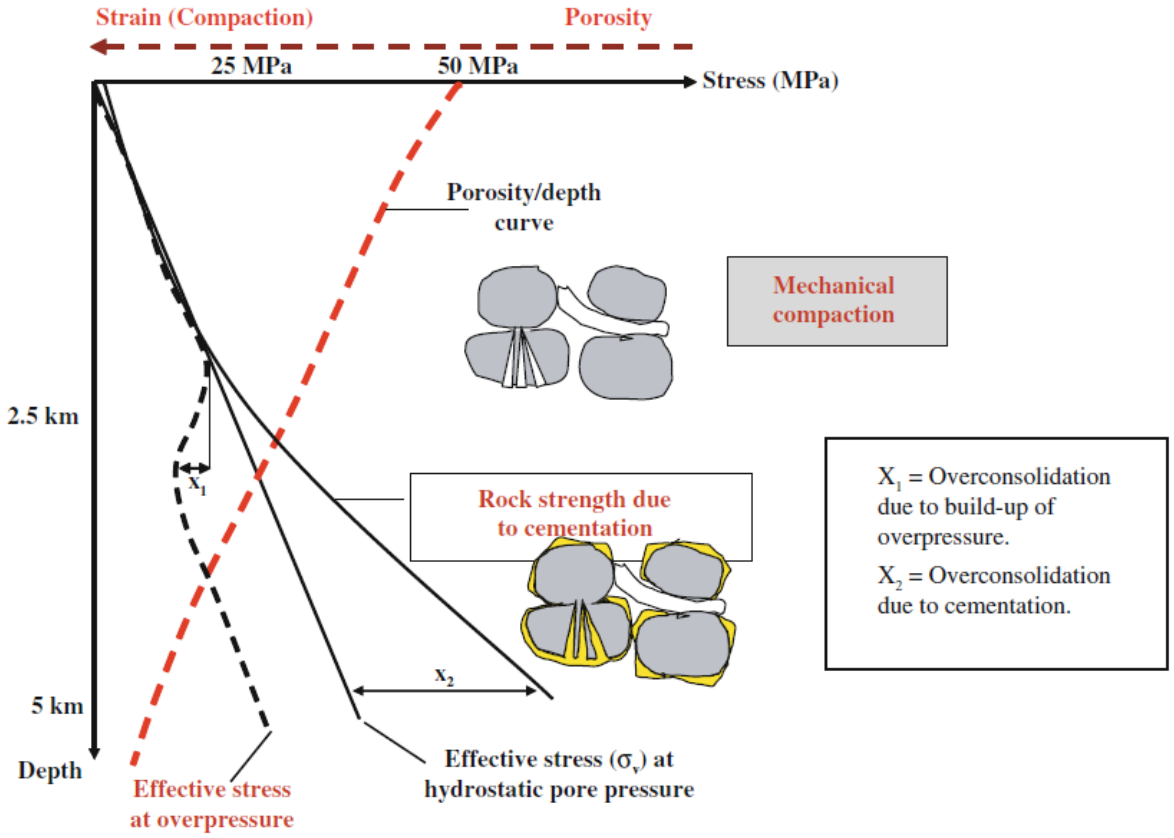

Figure 2.2. Sandstones firstly compact mechanically by grain reorientation and breakage as a response to the increase in effective stress. At 80-100°C (about 2 km burial depth) sandstones become cemented. Small amounts of quartz cement make the sandstone stiffer and overconsolidated, meaning that at greater depths mechanical compaction (strain) becomes almost negligible. (From Bjørlykke and Jahren, 2010**)**

2.2 Porosity loss models

Both mechanical compaction and quartz cementation are porosity reducing processes. However, they are controlled by different factors (effective stress and temperature, respectively) and this should be taken into account to predict porosity loss correctly.

Well log data from sedimentary basins can provide important information regarding compaction, as seen from the changes in the physical properties of the rocks with burial depth. In their study of the Etive Formation, Marcussen et al. (2010) concluded that at depths shallower than 2-2.5 km the compaction trend derived from log data showed good correlation with the experimental compaction in the laboratory. At greater depths, quartz cementation becomes the main controlling factor.

Several authors have developed different models that aim to predict porosity reduction in sandstones (Ehrenberg, 1990, Ramm, 1992, Walderhaug, 1996, Lander and Walderhaug, 1999). Porosity loss due to mechanical compaction can be greatly influenced by the textural and mineralogical composition of the rocks. At depths where quartz cementation is the main cause

of porosity loss, it is important to predict the occurrence of grain coatings that could prevent further porosity reduction.

2.2.1 Mechanical compaction model

Lander and Walderhaug (1999) proposed a compaction function to explain the intergranular volume loss as a function of effective stress (Figure 2.3), given by:

$$IGV = IGV_f + (\phi_0 + m_0 - IGV_f)e^{-\beta\sigma_{es}} \quad (2.1)$$

where *IGV* is the sum of pore space, cements and matrix material, and IGV_f is the stable packing configuration, both in volume fraction; ϕ_0 is the depositional porosity (volume fraction), m_0 is the initial proportion of matrix material (volume fraction), β is the exponential rate of *IGV* decline with effective stress (MPa^{-1}), and σ_{es} is the maximum effective stress (in MPa, hydrostatic pressure is assumed). This model is useful in predicting the porosity loss due to mechanical compaction, given that there is no quartz cementation in this domain.

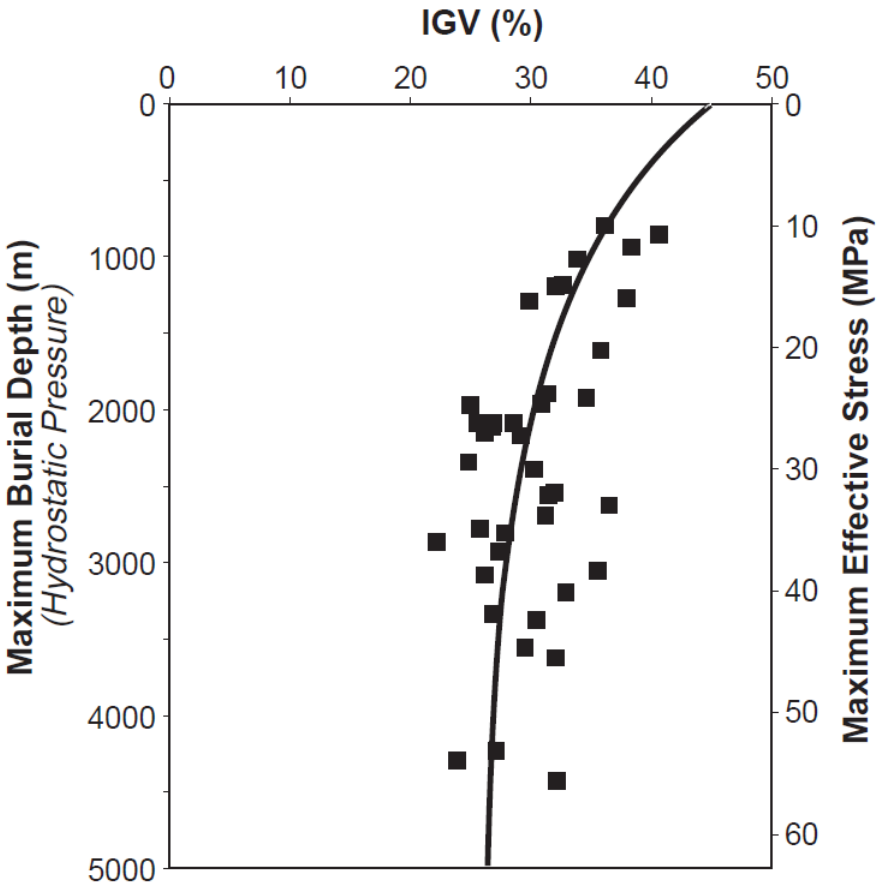

Figure 2.3. Lander and Walderhaug's compaction model. The data points are from Texas Eocene sandstones. (From Lander and Walderhaug, 1999)

2.2.2 Quartz cementation model

To predict quartz cementation, the model proposed by Walderhaug (1996) estimates the volume of quartz cement, Vq (in cm^3), precipitated in a 1 cm^3 volume of sandstone with quartz surface area A (in cm^2) during time t (in s), as:

$$Vq = \frac{MrAt}{\rho} \tag{2.2}$$

where M is the molar mass of quartz (60.09 g/mole) and ρ is the density of quartz (2.65 g/cm^3). The quartz precipitation rate, r (in moles/cm^2s), is expressed as a logarithmic function of temperature:

$$r = a10^{bT} \tag{2.3}$$

where T is temperature in °C, and a and b are constants set to $1.98x10^{-22}$ moles/cm^2s and $0.022°C^{-1}$, respectively, according to Walderhaug's (1994a) estimates.

If the volume of quartz cement, Vq, is to be calculated from the onset of quartz cementation for a certain period of time, and the temperature, T, changes with time, Equation 2.2 can be rewritten as:

$$Vq_n = Vq_{n-1} + \frac{Mr_{n-1}A_{n-1}dt}{\rho} \tag{2.4}$$

where dt is the time step, and the subscript n = 1,2,…,N indicates the volume of quartz cement for a corresponding time. When n = 1, the right side of Equation 2.4 deals with the initial values Vq_0, r_0 and A_0. Vq_0 is the volume of quartz cement at the start of quartz cementation, set to zero. The initial quartz precipitation rate, r_0, corresponds to the one at the initial temperature (i.e. the temperature when the quartz cementation started). The initial quartz surface area, A_0, is estimated by Walderhaug (1996), and can be expressed as:

$$A_0 = \frac{6(1-C)f}{D} \tag{2.5}$$

where D is grain size, f is the fraction of detrital quartz, and C represents the fraction of quartz grains coated by clay (clay coating factor).

At each time, the porosity and the quartz surface area are then given by:

$$\phi_n = \phi_0 - Vq_n \tag{2.6}$$

$$A_n = \frac{\phi_n A_0}{\phi_0} \tag{2.7}$$

where, in this case, ϕ_0 represents the porosity at the onset of quartz cementation.

Figure 2.4 illustrates the changes in fraction of quartz cement and porosity as a function of time for a modeled sandstone without clay coating (C=0), in a setting with a linear temperature increase of 2°C/Ma.

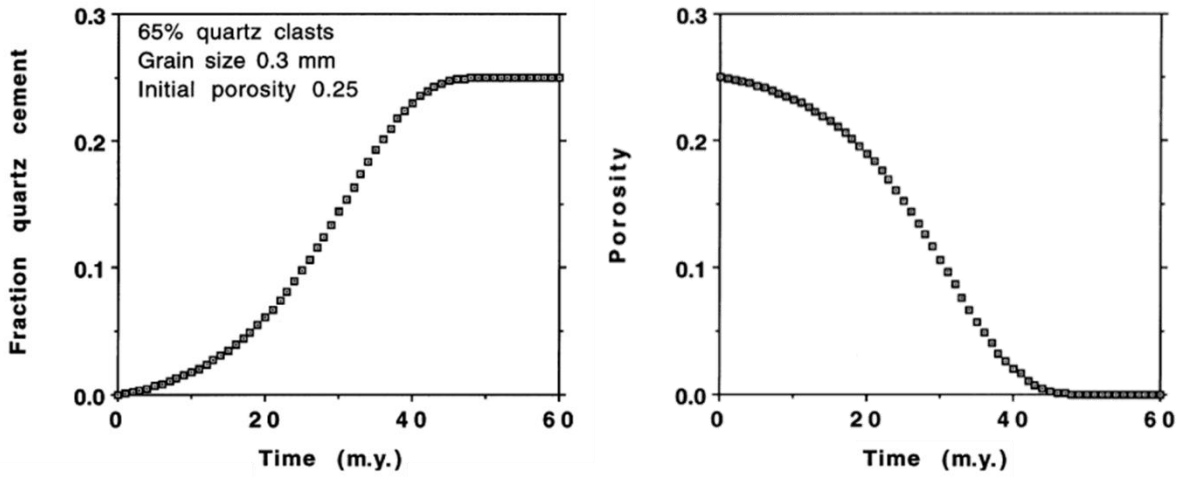

Figure 2.4. Fraction of quartz cement and porosity versus time for a sandstone with 65% quartz clasts, grain size of 0.3 mm, ϕ_0 equal to 0.25, and without clay coating. (m.y=Ma). (From Walderhaug, 1996)

Combining the two previously described models, it is possible to estimate the porosity reduction in sandstones that have been subjected to mechanical compaction and chemical compaction.

2.3 Rock physics diagnostics

The models derived from the rock physics diagnostics technique, introduced by Dvorkin and Nur (1996), allow to relate the elastic moduli of sediments and rocks to their porosity for different rock and sediment microstructures. Two models are presented: the friable-sand model and the contact-cement model.

2.3.1 The friable-sand model

The friable-sand model, or the unconsolidated line, describes the elastic moduli-porosity relation when sorting deteriorates (Figure 2.5). The dry elastic moduli of the well-sorted end point at critical porosity, K_{HM} and μ_{HM}, are given by the Hertz-Mindlin theory:

$$K_{HM} = \left[\frac{n^2(1-\phi_c)^2\mu^2}{18\pi^2(1-\nu)^2}P\right]^{1/3} \tag{2.8}$$

$$\mu_{HM} = \frac{5-4\nu}{5(2-\nu)}\left[\frac{3n^2(1-\phi_c)^2\mu^2}{2\pi^2(1-\nu)^2}P\right]^{1/3} \tag{2.9}$$

where ϕ_c is the critical porosity (or depositional porosity), P is the effective stress, and μ and ν are the shear modulus and Poisson's ratio of the mineral, respectively. The coordination number, n, is defined as the average number of contacts that each grain has with surrounding grains (Mavko et al., 2009).

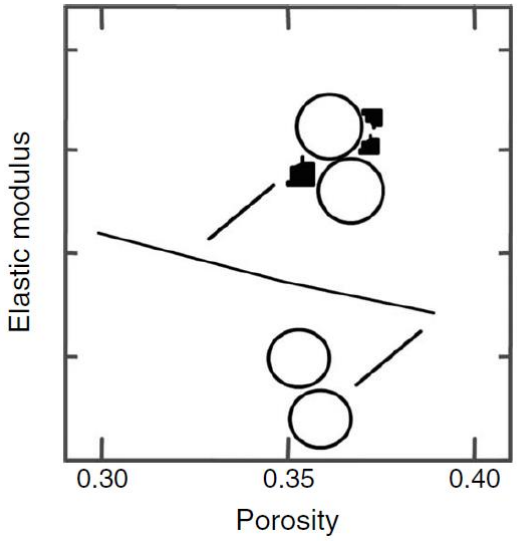

Figure 2.5. Schematic of the friable-sand model and corresponding sedimentologic variation. (From Avseth et al., 2010)

At zero porosity, the elastic dry moduli correspond to those of the mineral. The moduli of poorly sorted sands with porosities between zero and ϕ_c are interpolated between the mineral point and the well sorted point by means of Hashin-Strikman lower bound. At porosity ϕ, the concentration of pure solid phase that reduces the porosity in the rock is $1 - \phi/\phi_c$, and that of the original sphere pack phase is ϕ/ϕ_c (Avseth et al., 2010). The dry bulk modulus, K_{dry}, and shear modulus, μ_{dry}, of the friable-sand mixture are then defined as:

$$K_{dry} = \left[\frac{\frac{\phi}{\phi_c}}{K_{HM} + \frac{4}{3}\mu_{HM}} + \frac{1 - \frac{\phi}{\phi_c}}{K + \frac{4}{3}\mu_{HM}} \right]^{-1} - \frac{4}{3}\mu_{HM} \tag{2.10}$$

$$\mu_{dry} = \left[\frac{\frac{\phi}{\phi_c}}{\mu_{HM} + z} + \frac{1 - \frac{\phi}{\phi_c}}{\mu + z} \right]^{-1} - z \tag{2.11}$$

where K and μ are the bulk and shear moduli of the mineral, and z is defined as:

$$z = \frac{\mu_{HM}}{6}\left(\frac{9K_{HM} + 8\mu_{HM}}{K_{HM} + 2\mu_{HM}}\right) \tag{2.12}$$

The bulk modulus for a saturated scenario, K_{sat}, can be computed from Gassmann's fluid substitution ($\mu_{dry} = \mu_{sat}$), and together with the corresponding density for the given scenario, P-wave velocity, V_P, and S-wave velocity, V_S, can be estimated.

2.3.2 The contact-cement model

The contact-cement model assumes that porosity reduces from the initial porosity of a sand pack as result of the uniform deposition of cement on the surface of the grain (Avseth et al., 2010) (Figure 2.6). In this model, K_{dry} and μ_{dry} are defined as:

$$K_{dry} = \frac{n(1-\phi_c)M_c S_n}{6} \tag{2.13}$$

$$\mu_{dry} = \frac{3K_{dry}}{5} + \frac{3n(1-\phi_c)\mu_c S_\tau}{20} \tag{2.14}$$

where ϕ_c is the critical porosity and n is coordination number. The P-wave modulus of the cement material, M_c, is defined as $M_c = K_c + 4\mu_c/3$, where K_c and μ_c are the bulk and shear moduli of the cement material, respectively. The parameters S_n and S_τ are proportional to the normal and tangential stiffnesses, respectively, and are defined as:

$$S_n = A_n(\Lambda_n)\alpha^2 + B_n(\Lambda_n)\alpha + C_n(\Lambda_n) \tag{2.15}$$

$$S_\tau = A_\tau(\Lambda_\tau, \nu_s)\alpha^2 + B_\tau(\Lambda_\tau, \nu_s)\alpha + C_\tau(\Lambda_\tau, \nu_s) \tag{2.16}$$

where A_n, B_n, C_n, and A_τ, B_τ, C_τ are functions that relate the normal and tangential stiffnesses (Dvorkin and Nur, 1996), and α is given by:

$$\alpha = \left[\frac{\frac{2}{3}(\phi_c - \phi)}{1-\phi_c}\right]^{0.5} \tag{2.17}$$

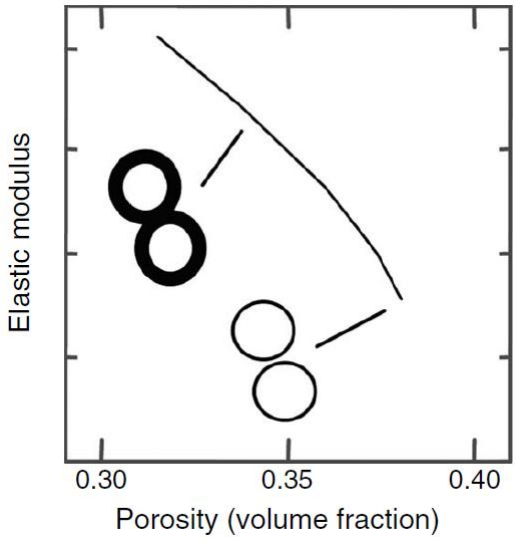

Figure 2.6. Schematic of the contact-cement model and the corresponding diagenetic transformation. (From Avseth et al., 2010)

CHAPTER 3 GEOLOGICAL SETTING

The study area for this investigation comprises the Norwegian North Sea and the Norwegian Sea. The extension of both areas is shown in Figure 3.1.

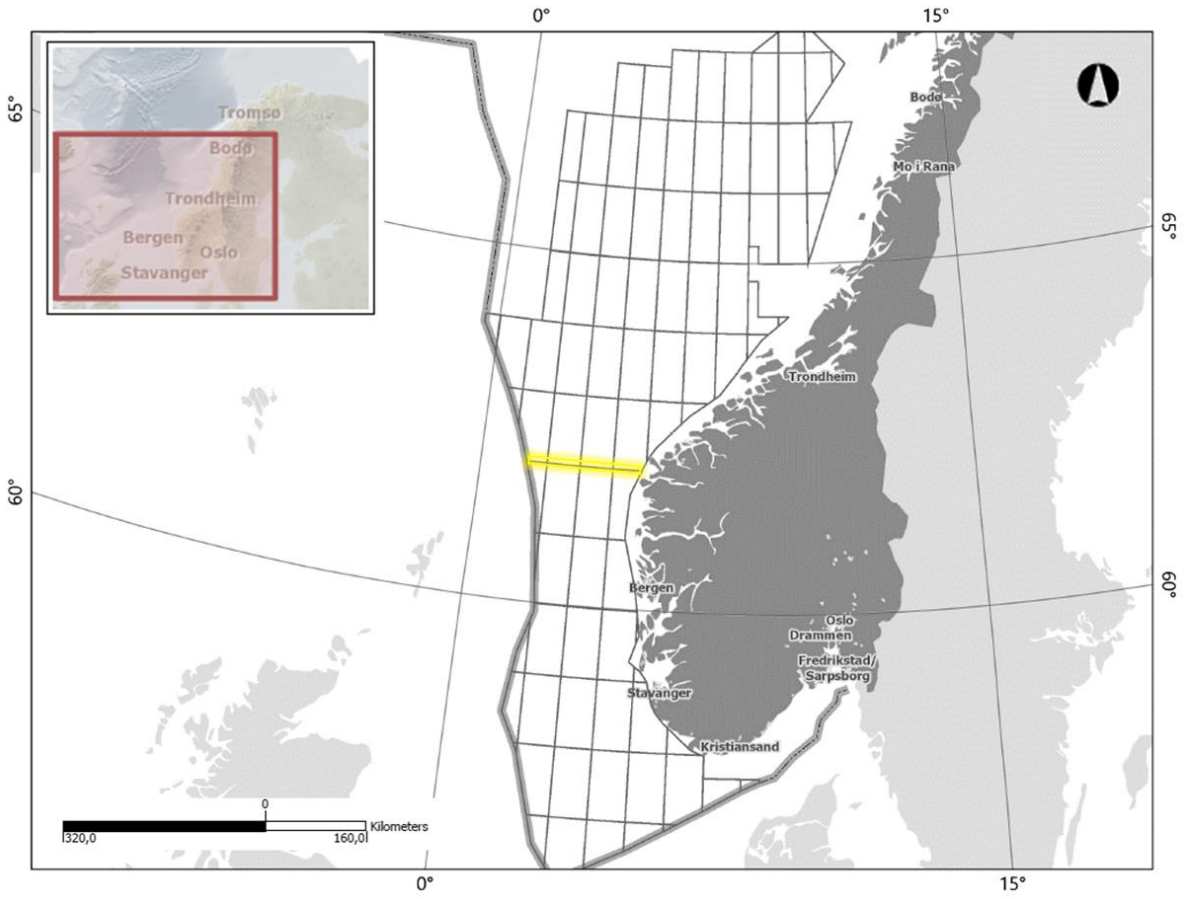

Figure 3.1. Map of the Norwegian Shelf showing the extension of the Norwegian North Sea and the Norwegian Sea. The yellow line represents the limit between both areas (North Sea to the South and Norwegian Sea to the North). The bold gray line denotes the limit of the Norwegian Shelf. (With data from NPD FactMaps)

3.1 Norwegian North Sea

The structural framework of the North Sea is mainly the result of two major rift episodes, one during Permian to Early Triassic and a second one during Late Jurassic to Early Cretaceous. After the rifting ceased, it was followed by thermal subsidence (Deegan and Scull, 1977, Vollset and Doré, 1984).

At the beginning of the Middle Jurassic, volcanic updoming took place in the North Sea and deltaic systems built outwards radially from the updomed area, depositing the sands that comprise the Brent Group in the northern area (East Shetland Basin, North Viking Graben, Horda Platform) (Vollset and Doré, 1984). As a consequence of the last rifting episode, the Brent Group sediments are buried to very different depths (Marcussen et al., 2010).

The Brent Group consists of five formations: Broom (base), Rannoch, Etive, Ness, and Tarbert (top) (Vollset and Doré, 1984), which are considered to be part of a major river-delta system (Helland-Hansen et al., 1992).

For this study, the Etive Formation is the most relevant in the North Sea area. The Etive Formation consists mainly of fine to coarse sandstones, and is interpreted as upper shoreface, barrier bar, mouth bar and distributary channel deposits of Bajocian age (Vollset and Doré, 1984).

3.2 Norwegian Sea

The Caledonian Orogeny and the break-up of the North Atlantic divide the tectonic history of the Norwegian Sea into three major events (Blystad et al., 1995): 1) Final closure of the Iapetus Ocean during the Caledonian Orogeny (Late Silurian/Early Devonian), 2) A series of extensional deformation episodes, culminating with the continental separation between Eurasia and Greenland (Late Devonian to Paleocene), and 3) Active seafloor spreading between Eurasia and Greenland (Earliest Eocene to Present).

During the Early Jurassic (Sinemurian/Pliensbachian), prominent, NNE trending faults detached in Triassic evaporites. When the growth faulting ceased, the Fangst Group sediments were deposited during a quiet episode through the Middle Jurassic (Blystad et al., 1995).

The Fangst Group is a sand-dominated regressive sequence contemporaneous with the Brent Group of the northern North Sea (Ehrenberg, 1990). The Fangst Group consists of three formations: Ile (base), Not, and Garn (top), and is present over most of the Haltenbanken and Trænabanken area (Dalland et al., 1988).

In the Norwegian Sea area, the Garn Formation is the most relevant for this study. The Garn Formation consists of medium to coarse-grained, moderately to well-sorted sandstones, and is interpreted as progradations of braided delta lobes (Dalland et al., 1988).

Figure 3.2 shows a lithostratigraphic section of Jurassic formations in the Northern North Sea and in the Haltenbanken.

During the late Cenozoic, mainland Norway and the eastern part of the Norwegian Shelf experienced uplift and erosion (Hansen, 1996). Figure 3.3 shows the iso-uplift curves for quantified net uplift and erosion on the Norwegian Shelf south of 66°N, constructed by Hansen (1996) from sonic transit times of shale.

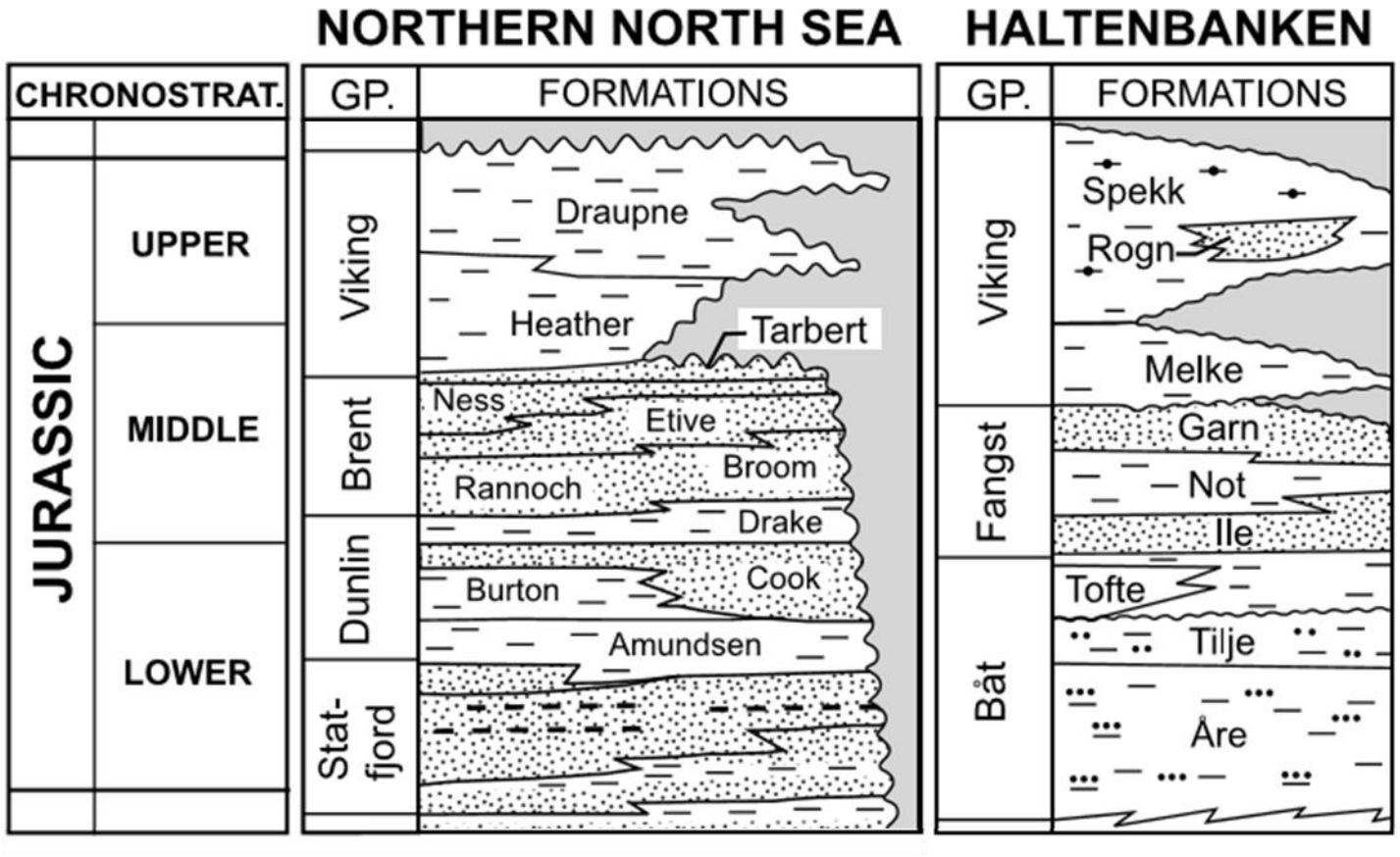

Figure 3.2. Lithostratigraphic section of Jurassic formations in the Northern North Sea and in the Haltenbanken. (Modified from Storvoll et al., 2005)

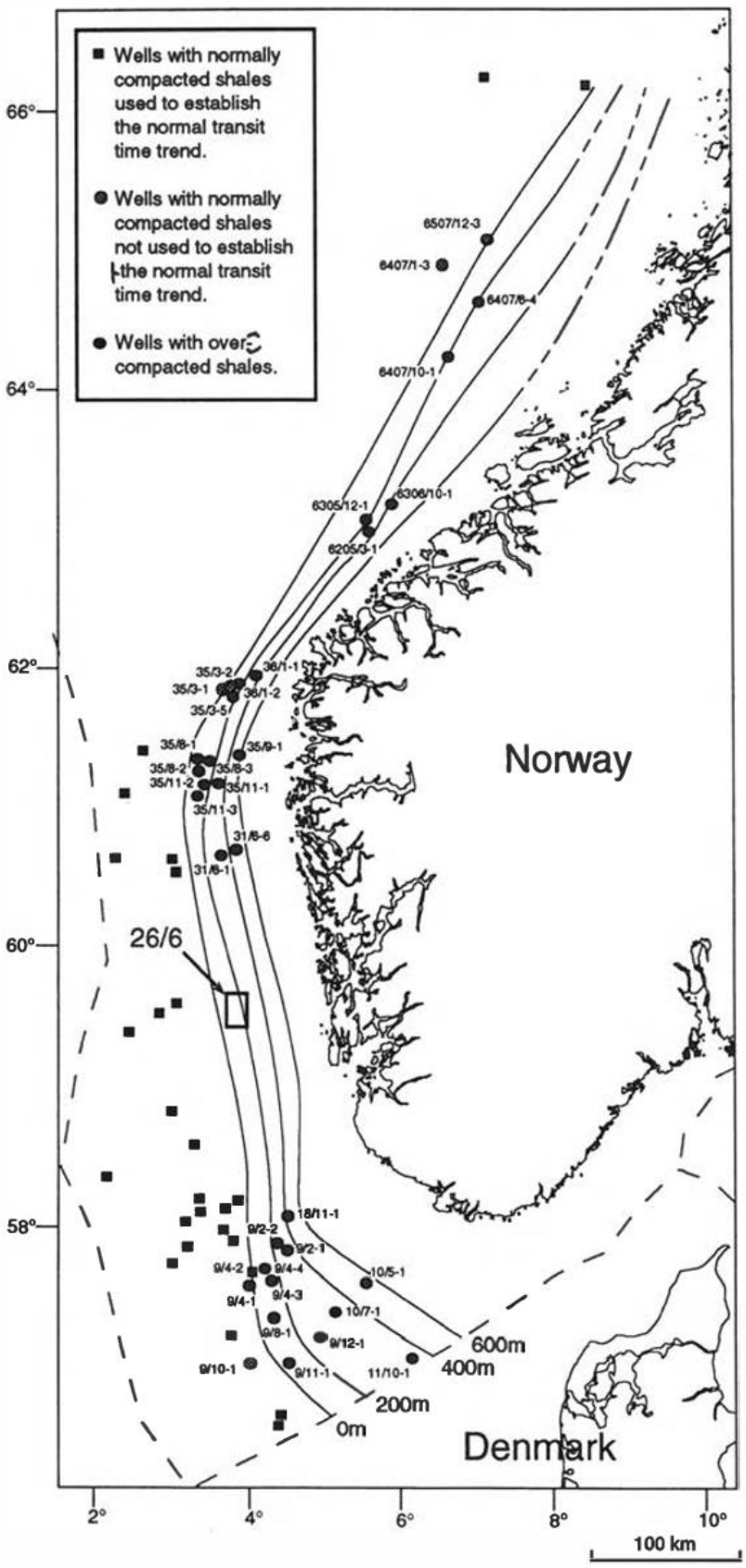

Figure 3.3. Iso-uplift curves (in meters) for quantified net uplift and erosion on the Norwegian Shelf. (From Hansen, 1996)

CHAPTER 4 DATA AND METHODOLOGY

4.1 Data

15 wells from the northern North Sea and 15 wells from the Norwegian Sea were selected and analyzed with respect to petrophysical properties available from the logs. In the case of the North Sea, 7 wells corresponded to the ones studied by Marcussen et al. in 2010. Hansen's study (1996) discussed in the previous chapter was taken into account to select wells that were not in an uplifted area. The studied intervals belonged to the sandstones of the Etive Formation (North Sea) and the Garn Formation (Norwegian Sea).

Figures 4.1 and 4.2 show the location of the wells in the North Sea and in the Norwegian Sea, respectively.

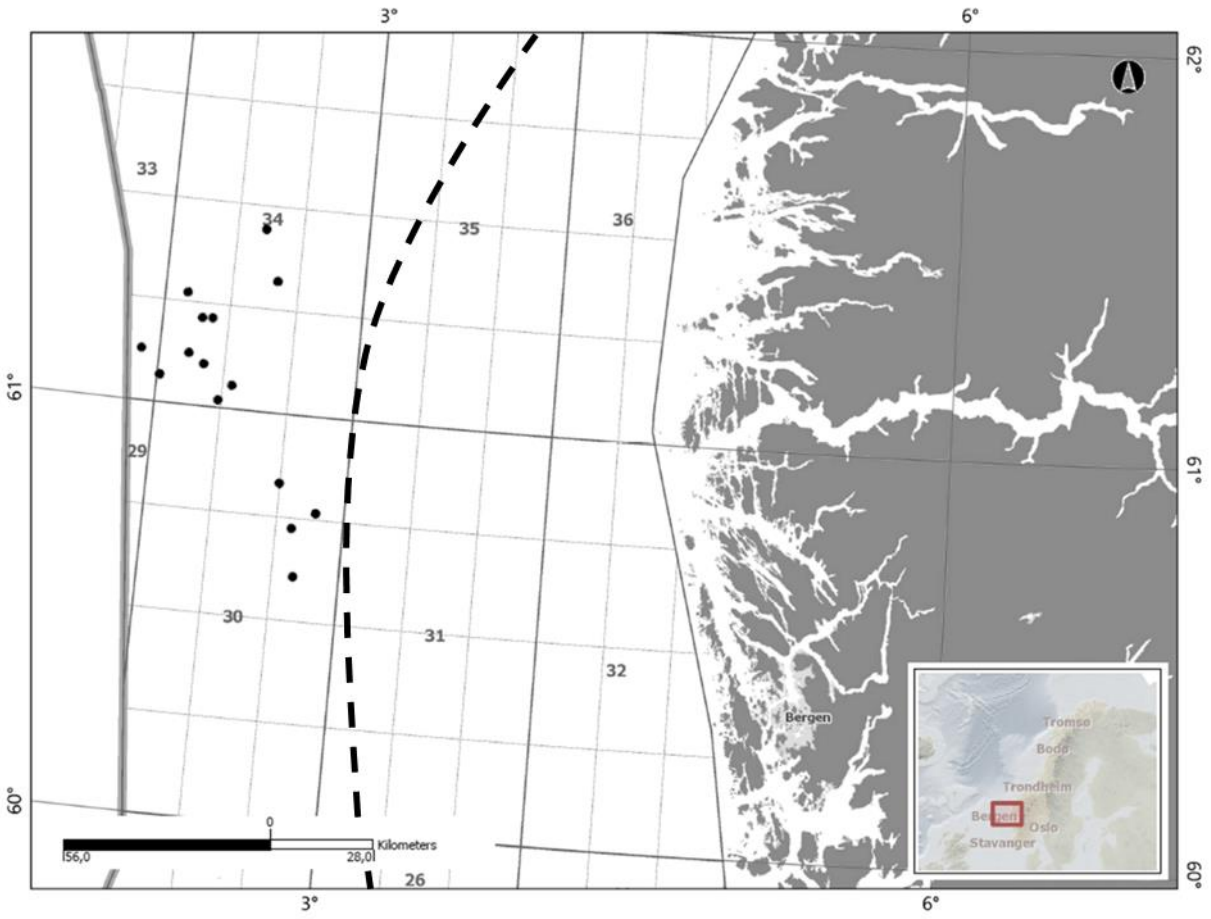

Figure 4.1. Location of the studied wells in the North Sea. The black dashed line represents the 0 m iso-uplift curve from Hansen (1996). (With data from NPD's FactMaps)

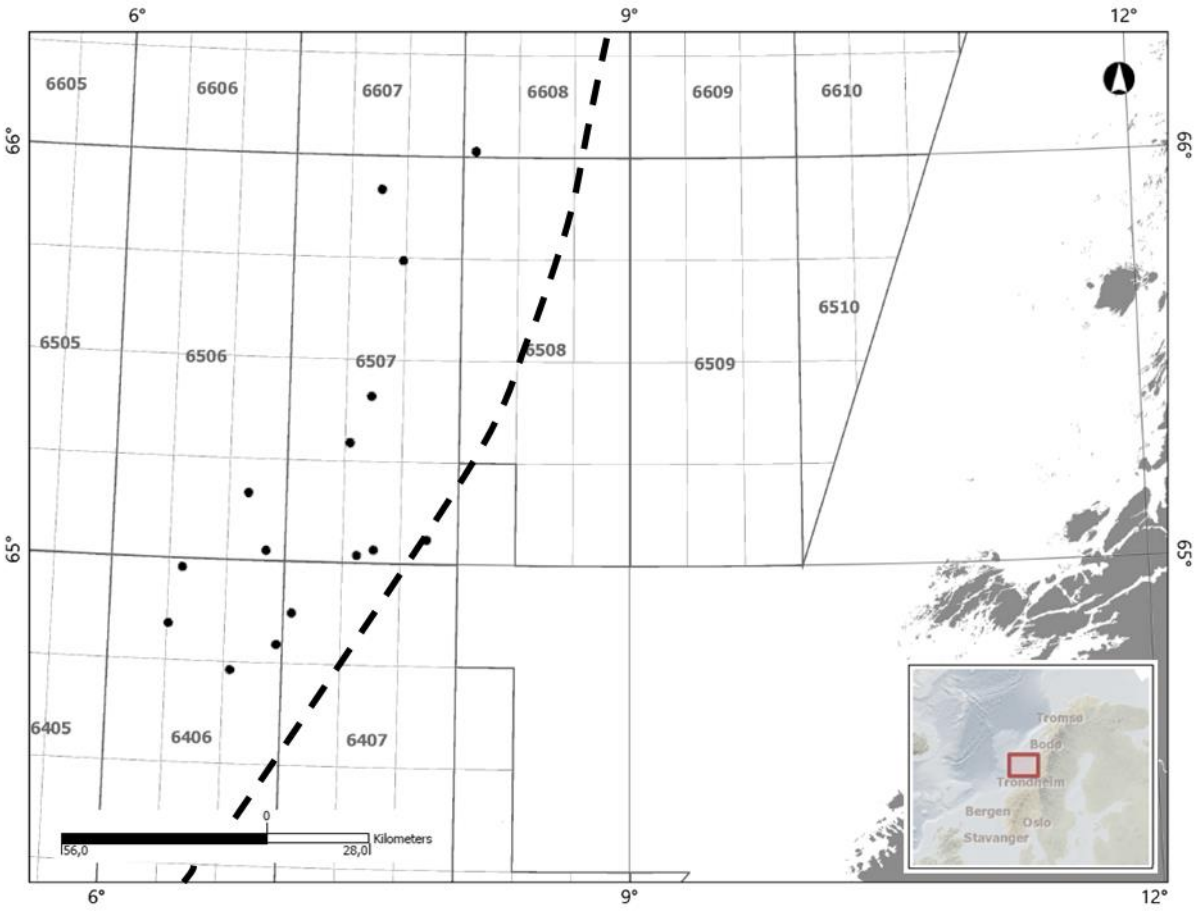

Figure 4.2. Location of the studied wells in the Norwegian Sea. The black dashed line represents the 0 m iso-uplift curve from Hansen (1996). (With data from NPD's FactMaps)

To perform an adequate comparison between both areas, the wells were also selected so that the depths (measured from sea floor) of the Etive and Garn formations were approximately the same. The top depth, bottom depth and formation thickness for each well analyzed in this study are summarized in Tables 4.1 (Etive Fm.) and 4.2 (Garn Fm.).

4.2 Temperature calculations

To observe the overall trends of present day temperature as a function of depth for the North Sea and the Norwegian Sea, the bottom hole temperature (BHT) versus depth was plotted for all the wells (Figure 4.3).

The bottom water temperature (BWT) was calculated for each well and, subsequently, the temperature gradient according to Equation 4.1:

$$G_T = \frac{BHT - BWT}{TVD_{MSF}} \tag{4.1}$$

where TVD_{MSF} is the total true vertical depth of the well measured from sea floor, and G_T is the temperature gradient in °C/km. The temperature gradients of the studied wells ranged between

24-48°C/km. Figure 4.4 shows the temperature/depth trend for a well computed from its temperature gradient.

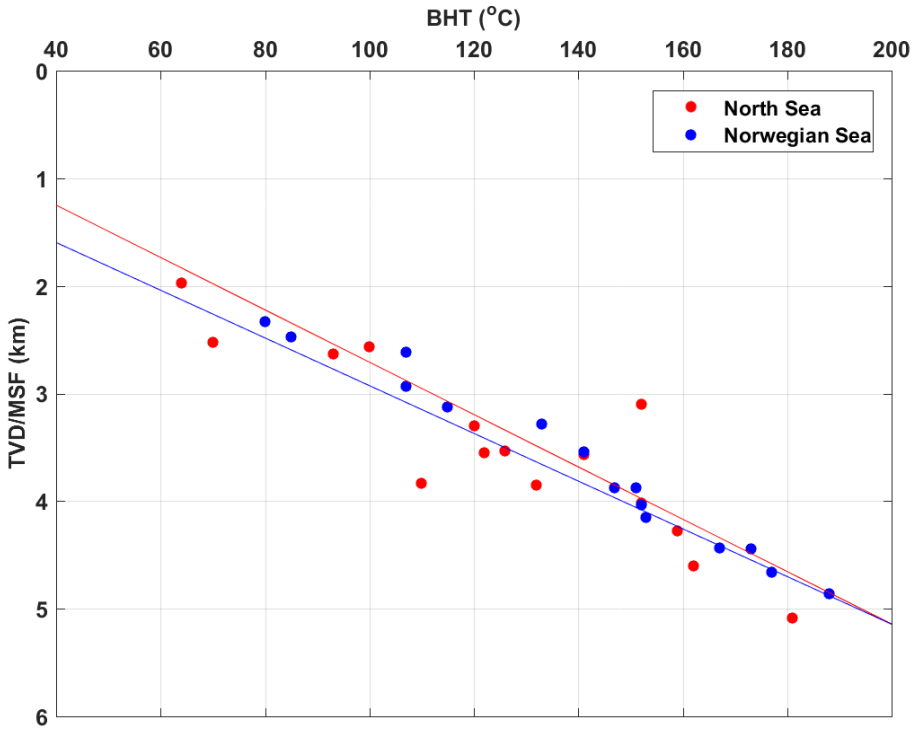

Figure 4.3. Bottom hole temperature (BHT) versus final vertical depth for all the studied wells in the North Sea (red) and the Norwegian Sea (blue). Similar trends are observed for both areas.

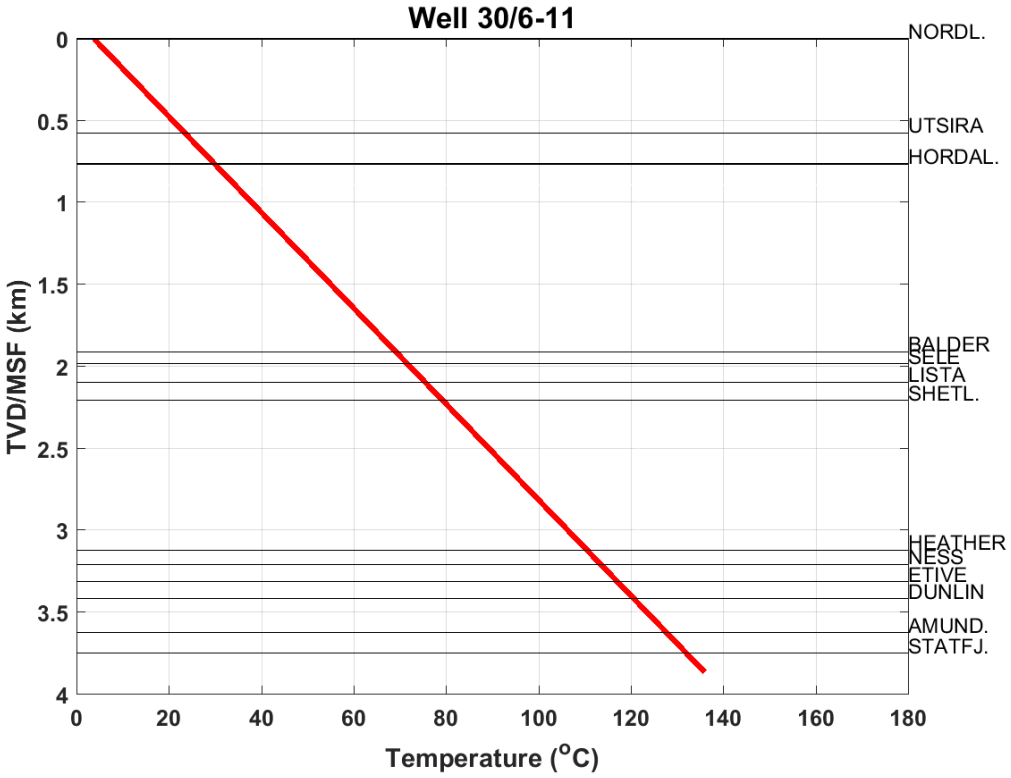

Figure 4.4. Temperature versus depth for well 30/6-11 with a temperature gradient of 33°C/km. Formation/Group tops are indicated.

Table 4.1. Top depth, bottom depth and thickness of the Etive Fm. from the wells studied in the North Sea (with information from the Norwegian Petroleum Directorate's FactPages).

Well	Top Depth (mRSF)	Bottom Depth (mRSF)	Thickness (m)
34/10-9	1609	1640	31
34/10-3	1813	1837	24
34/7-12	2036	2053	17
30/6-10	2409	2443	34
30/3-4	2686	2762	76
34/10-17	2774	2777	3
34/10-2	2912	2925	13
33/12-7	3072	3085	13
30/6-11	3313	3415	102
34/8-6	3324.5	3357.5	33
34/10-21	3332	3338	6
30/2-2	3918	3923	5
34/10-23	4079	4123	44
34/11-4	4120	4135	15
34/8-7	4341	4356	15

Table 4.2. Top depth, bottom depth and thickness of the Garn Fm. from the wells studied in the Norwegian Sea (with information from the Norwegian Petroleum Directorate's FactPages).

Well	Top Depth (mRSF)	Bottom Depth (mRSF)	Thickness (m)
6507/12-3	1706	1749	43
6507/8-6	1717	1741	24
6507/11-3	2096	2141	45
6608/10-2	2181	2214	33
6507/8-7	2464	2492	28
6507/11-6	2715	2762	47
6507/5-1	3033.5	3087.5	54
6507/2-2	3266	3291	25
6407/1-3	3285	3389	104
6406/3-6	3353	3470	117
6506/12-3	3499	3585	86
6506/12-6	3933	3978	45
6406/6-1	3936	4007	71
6406/2-7	4241	4257	16
6406/2-3	4233	4320	87

4.3 Stress calculations

For each well, the lithostatic stress, σ, and the hydrostatic pressure, p_h, were calculated according to Equations 4.2 and 4.3:

$$\sigma(z) = g \int_0^z \rho_b dz \tag{4.2}$$

$$p_h(z) = g \int_0^z \rho_w dz \tag{4.3}$$

where g is gravity, assumed to be 9.81 m/s^2, ρ_b is the bulk density from the density log, ρ_w is the water density, set to a constant value of 1.03 g/cm^3, and Z is the final vertical depth below sea floor.

A differential stress was then computed as:

$$\sigma_{diff} = \sigma(z) - p_h(z) \tag{4.4}$$

Figure 4.5 shows the lithostatic stress, the hydrostatic pressure and the differential stress for one of the wells in the North Sea.

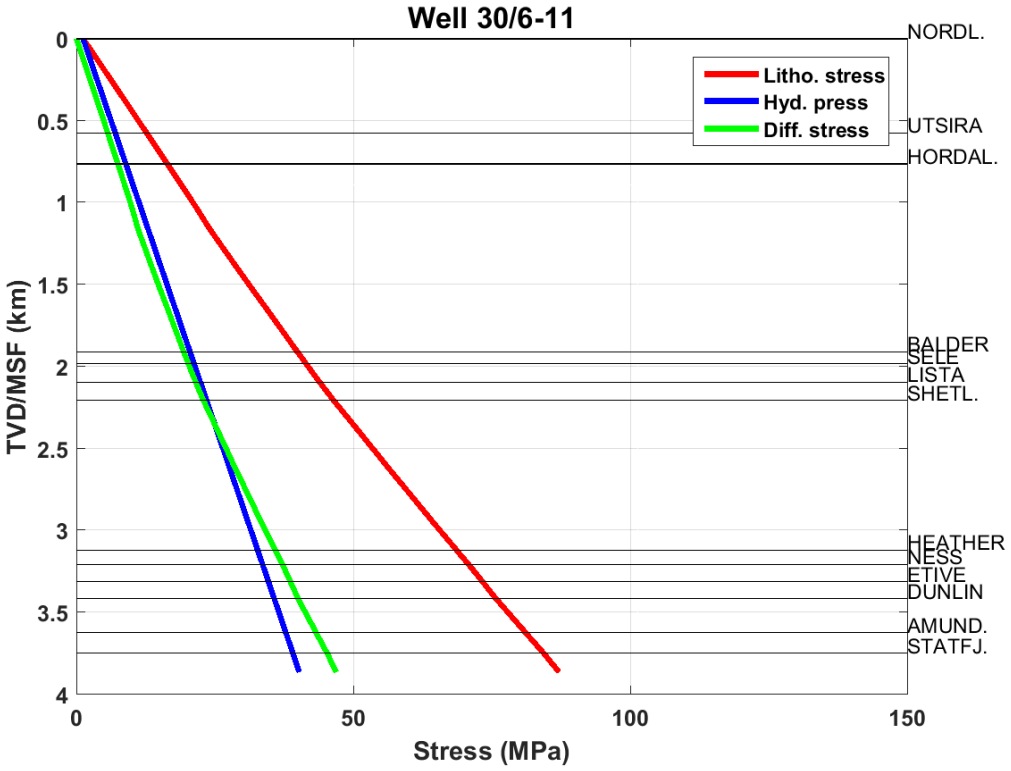

Figure 4.5. Lithostatic stress (red), hydrostatic pressure (blue) and differential stress (green) for well 30/6-11.

4.4 Porosity calculations

Considering that several of the studied wells contained gas or condensate, the porosity was estimated from density and neutron logs. The aim of this was to reduce uncertainties related to the unknown fluid density, which is an input for standard porosity calculations from bulk density.

Equation 4.5 gives the estimated porosity, ϕ, using density and neutron measurements:

$$\phi = \sqrt{\frac{\phi_N^2 + \phi_D^2}{2}} \tag{4.5}$$

where ϕ_N is the neutron porosity corrected for the appropriate lithology (in this case sandstone), and ϕ_D is the density porosity calculated as:

$$\phi_D = \frac{\rho_{ma} - \rho_b}{\rho_{ma} - \rho_{fl}} \tag{4.6}$$

where ρ_{ma} is the matrix density, in this case 2.65 g/cm^3 (quartz density), ρ_b is the bulk density read from the log, and ρ_{fl} is the density of the fluid, which is assumed to be water, with a value of 1.03 g/cm^3.

4.4.1 Porosity loss modeling

Mechanical compaction and quartz cementation was simulated in order to model the porosity loss with depth for the Etive and Garn formations, and compare it with the resulting trends from the previous porosity calculations.

The mechanical compaction simulation was performed using the compaction function proposed by Lander and Walderhaug (1999), presented in section 2.2.1.

The values of IGV_f for the Etive and Garn sandstones were assumed to be 0.28 and 0.26, respectively, in accordance with the values documented by Marcussen et al. (2010) and Ehrenberg (1990). The depositional porosity, ϕ_0, was set to be 0.40 as a reasonable value for sandstones (Nur et al., 1998), and m_0 was set to 0, the sum of these two variables constitutes the initial *IGV* (i.e. *IGV* at zero effective stress). The value of β was fixed to 0.06 MPa^{-1}, as that documented by Lander and Walderhaug (1999) to provide good correspondence between model predictions and measurements in sandstones. The effective stress (in this case, the differential stress assuming hydrostatic pressure) ranged between 0-55 MPa, with a step of 0.1 MPa.

The quartz cementation was simulated by means of the model proposed by Walderhaug (1996), discussed in section 2.2.2.

Both for the Etive and Garn sandstones, the temperature at the start of quartz cementation was set to 75°C, given that previous studies for the same sandstones have shown that quartz cementation takes place when temperatures reach 70-80°C (Walderhaug, 1994b, Marcussen et al., 2010). These temperatures correspond to a burial depth around 2 km for the studied areas

(Ehrenberg, 1990, Storvoll et al., 2005, Marcussen et al., 2010). The fraction of detrital quartz, *f*, ranged between 0.64-0.65, and a clay coating factor, *C*, of 0.1 was assumed. Grain sizes, *D*, varied between 0.2-0.6 mm for the Etive sandstones, and between 0.2-0.4 mm for the Garn sandstones, according to the studies performed by Marcussen et al. (2010) and Ehrenberg (1990), respectively.

The temperature history for each Formation was assumed from temperature versus time curves proposed by Walderhaug (1994b) (Figure 4.6). For different periods of time, the temperature increase rates varied between 0.4-5°C/Ma and 0.3-6°C/Ma for the Etive Fm. and the Garn Fm., respectively.

Additionally, Walderhaug's model indicates the quartz cementation and the porosity loss as a function of time. To express the porosity loss as a function of depth, burial history curves presented by Walderhaug (1994b) were used to convert the geological time to depth below sea floor (Figure 4.7). The burial rates varied between 15-75 m/Ma and 5-220 m/Ma for the Etive Fm. and the Garn Fm., respectively.

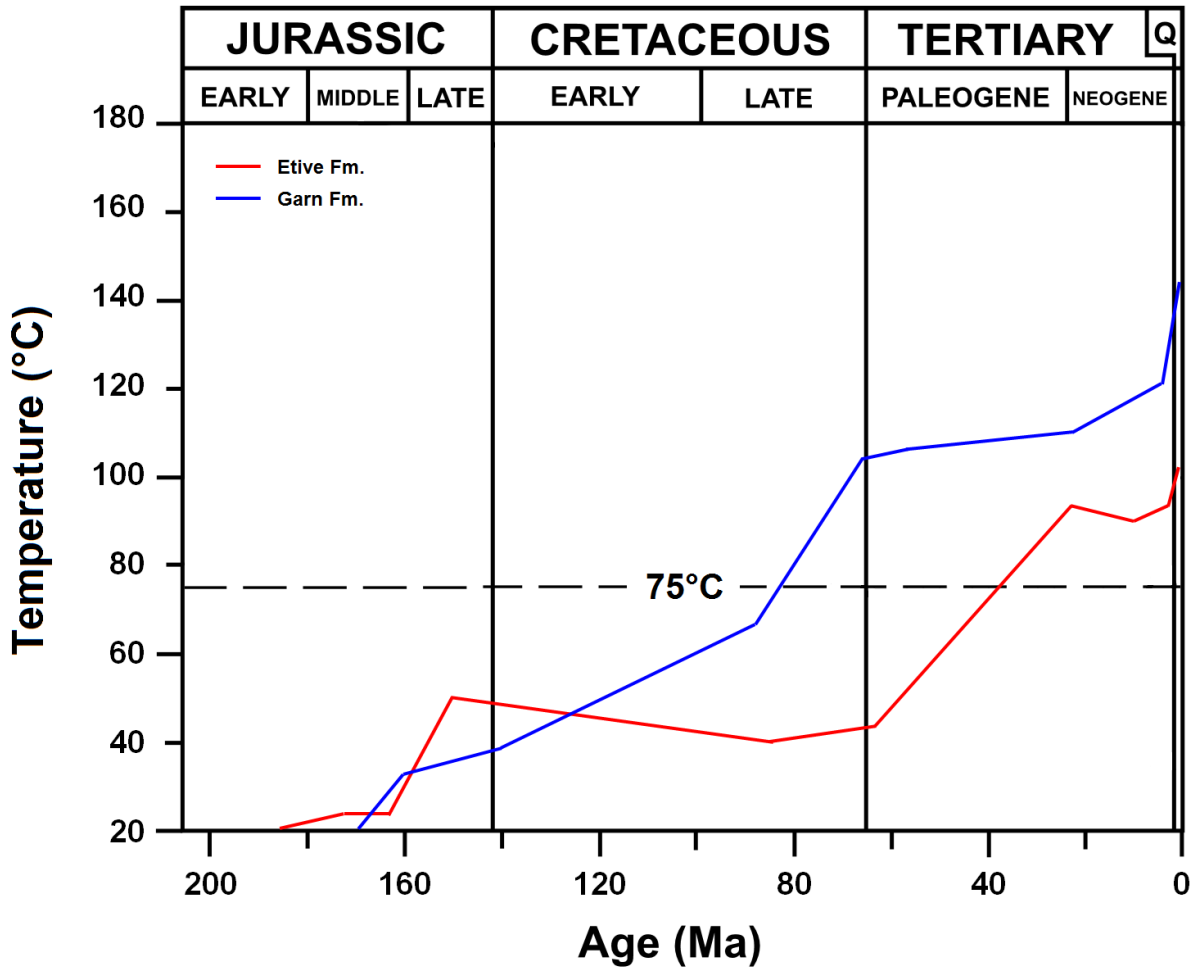

Figure 4.6. Temperature versus time curves for the Etive Fm. (red) and the Garn Fm. (blue). (Modified from Storvoll et al. (2005) with data digitized from Walderhaug (1994b))

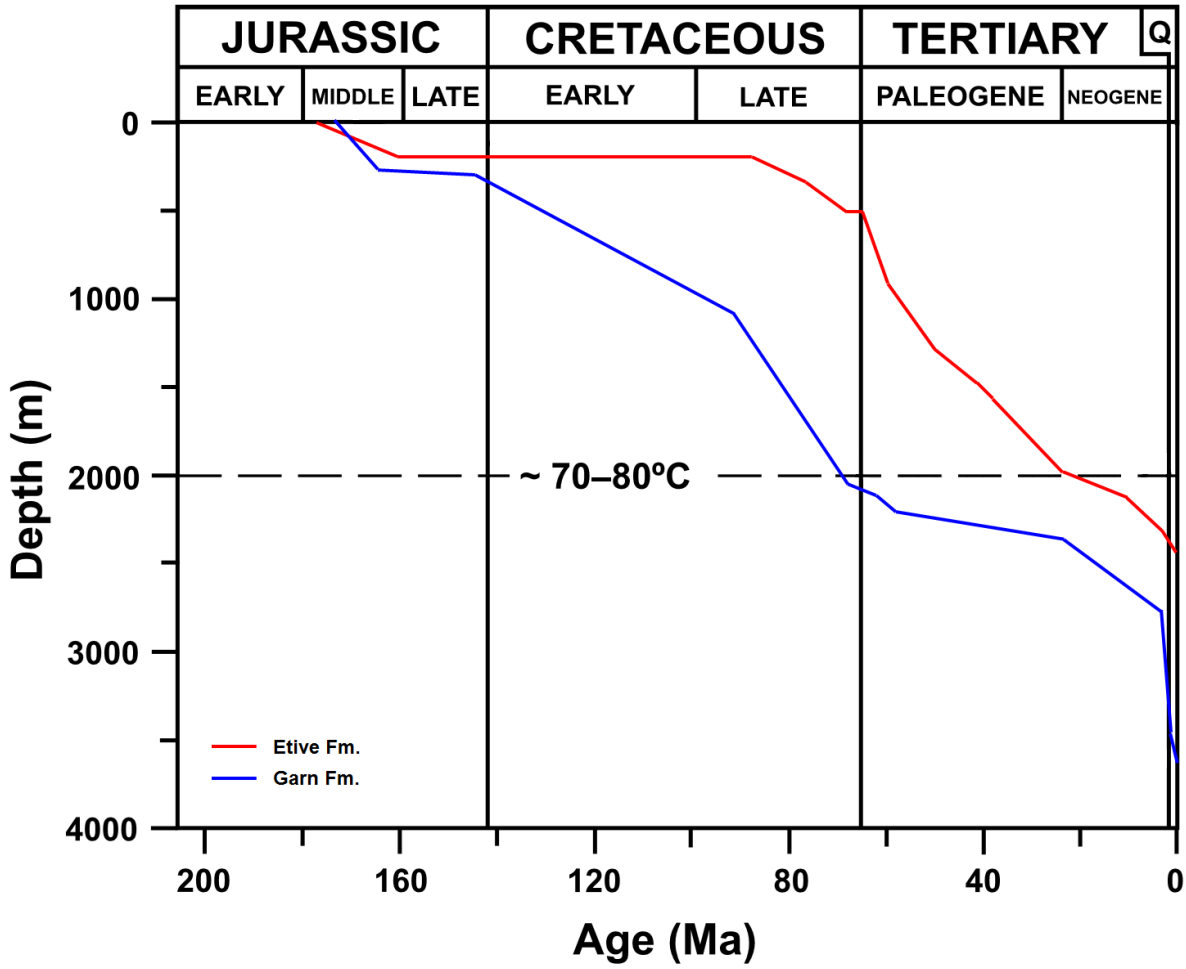

Figure 4.7. Burial history curves for the Etive Fm. (red) and the Garn Fm. (blue). Depth is in meters below sea floor. (Modified from Storvoll et al. (2005) with data digitized from Walderhaug (1994b))

It is important to note, however, that these curves (temperature history and burial history) were constructed with data from a specific well where the given Formation was encountered, and might not be representative for the same Formation deposited in a different area further away from the reference well. Because of this, and due to the lack of further information about temperature and burial history for the studied sandstones, the temperature and burial were assumed to increase linearly and with a constant rate from the start of chemical compaction until present day. From the curves in Figures 4.6 and 4.7, this resulted in temperature increase rates of 0.65 and 0.82°C/Ma, and burial rates of 22 and 25 m/Ma for the Etive and the Garn formations, respectively.

4.5 Formation water resistivity

Gelius and Wang (2008) expressed the brine conductivity, σ_w, as a function of temperature and salinity given by:

$$\sigma_w(s,T) = \sigma_w(s_0,T_0) + \Delta\sigma_w \tag{4.7}$$

with

$$\Delta\sigma_w = 0.0958(s - s_0) + 0.00462(T \cdot s - T_0 \cdot s_0) - 0.26 \cdot 10^{-5}(T^2 \cdot s - T_0^2 \cdot s_0) - \frac{2.24 \cdot 10^{-3}(2.36 + 0.099T)}{(1.0 + 2.8 \cdot 10^{-2}\sqrt{s})} s^{3/2} + \frac{2.24 \cdot 10^{-3}(2.36 + 0.099T_0)}{(1.0 + 2.8 \cdot 10^{-2}\sqrt{s_0})} s_0^{3/2} \tag{4.8}$$

where $\sigma_w(s_0,T_0)$ represents the brine conductivity at initial salinity (s_0) and temperature (T_0). For this study, these initial values are assumed to be 35 kppm for salinity, 20°C for temperature, and 5 S/m for conductivity.

The values of temperature, *T*, are those calculated in section 4.2 by means of the temperature gradient. In the case of salinity, *s*, the formation water salinities from four wells in the North Sea were available from water analysis reports in NPD's FactPages, and these values ranged between 31.5-45.3 kppm (Table 4.3). For the rest of the wells, a constant value of 34 kppm was used.

Table 4.3. Formation water salinities from wells where water analysis reports were available.

Well	Formation water salinity (kppm)
34/10-3	42.3
34/7-12	31.5
34/10-17	33.2
34/10-2	45.3

Once brine conductivity was calculated by means of Equation 4.7, formation water resistivity, R_w, was computed as:

$$R_w = 1/\sigma_w \tag{4.9}$$

4.6 Clay volume calculations

The clay volume was calculated from the gamma ray log and the neutron-density logs. The clay volume (fractional) from neutron and density measurements is given by:

$$V_{cl_{N-D}} = \frac{\phi_N - \phi_D}{\phi_{N_{cl}} - \phi_{D_{cl}}} \tag{4.10}$$

where ϕ_N is the neutron porosity corrected for the appropriate lithology (in this case, sandstone), and ϕ_D is the density porosity calculated as in Equation 4.6. ϕ_{Ncl} is the neutron log reading in 100% clay, set to 0.40, and ϕ_{Dcl} is the apparent density porosity in clay, set to 0.

From gamma ray measurements, the clay volume (fractional) can be expressed as:

$$V_{cl_{GR}} = \frac{GR_{log} - GR_{min}}{GR_{max} - GR_{min}} \tag{4.11}$$

where GR_{log} is the gamma ray log reading in the zone of interest, GR_{min} is the gamma ray log reading in a clean zone having no clay, and GR_{max} is the gamma ray log reading in a zone composed by 100% clay. The values of GR_{min} and GR_{max} were adjusted for each well at the depths of interest (corresponding to Jurassic formations). For the North Sea wells, the GR_{min} and GR_{max} values ranged between 15-60 and 85-150, respectively. For the Norwegian Sea wells, the GR_{min} and GR_{max} values ranged between 15-35 and 100-150, respectively.

The final clay volume was computed as an average from the two previously described methods:

$$V_{cl} = \frac{V_{cl_{N-D}} + V_{cl_{GR}}}{2} \tag{4.12}$$

The main reason for this approach is that V_{clGR} is affected by the presence of other minerals commonly find in sandstones and that are heavier than quartz (e.g. mica), meaning that the volume of clay could be overestimated. On the other hand, $V_{clN\text{-}D}$ is affected by the presence of gas, given the greater separation of the neutron and density curves, and can result in an underestimation of the clay volume.

Of interest for this study are the sandstones from the Etive and Garn formations with V_{cl} less than 0.05.

4.7 Water saturation

Since the interest of this study are clean sandstones, water saturation was computed from Archie's equation (1952):

$$S_w = \left(\frac{a\, R_w}{\phi^m\, R_t}\right)^{\frac{1}{n}} \tag{4.13}$$

where the constant a is the tortuosity factor (usually close to 1), R_w is the formation water resistivity, ϕ is porosity, m is the cementation exponent, R_t is the true resistivity of the formation, and n is the saturation exponent.

The values of a, m and n were set to 1, 2 and 2, respectively, as those that can be representative for sandstones (Archie, 1952). The values of porosity, ϕ, and formation water resistivity, R_w, are those calculated in sections 4.4 and 4.5, respectively. The readings from the deep resistivity log, R_d, were assumed to be representative of the true resistivity of the formation, R_t.

4.8 Fluid properties – Density and bulk modulus

Most of the studied wells contained hydrocarbons, either gas or oil, or a combination of both. Only one well from the North Sea and three wells from the Norwegian Sea did not encounter hydrocarbons according to the information available from NPD's FactPages.

Before performing fluid substitution to a water saturated scenario for the wells containing hydrocarbons, the densities and the bulk moduli of the involved fluids were calculated for the intervals of interest (Etive and Garn formations). These calculations are based on those from Batzle and Wang (1992) to predict the seismic properties of pore fluids.

These calculations also take into account the pressure and temperature conditions. For this purpose, the pore pressure was assumed to be equal to the mean hydrostatic pressure in the interval of interest. The temperature values corresponded to the mean temperature (from section 4.2) of the corresponding interval. Additionally, there are other key input properties to calculate the densities and the bulk moduli of the fluids: salinity for brines, gravity for gases, and API gravity and gas-oil ratio for oils.

The brine salinities were the same used in section 4.5. For some of the gas wells, the gas gravity was available from completion reports, or it was calculated from the fluid composition analyses; these values ranged between 0.645 and 0.770. For the wells where this information was not available, an average gravity of 0.695 was used. The API gravity was available (from NPD's FactPages and completion reports) for some of the studied wells containing oil, and the values ranged between 28 and 48. If not available, a constant value of 40 API was used.

Appendix A summarizes the pore fluid properties from the intervals of interest (Etive Fm. and Garn Fm.) in the studied wells from the North Sea and the Norwegian Sea, respectively. The average formation water resistivities calculated in section 4.5 are also included.

4.9 Fluid substitution

To perform a sensible comparison and correlation with the data from all the wells, it is important to take them to the same scenario, a 100% water saturated scenario in this case. Fluid substitution was carried out for all the wells with hydrocarbon content.

Following the calculations of the bulk moduli of the involved fluids, the bulk modulus of the fluid mixture, K_{mix}, was calculated for each well, according to:

$$K_{mix} = \left(\frac{1 - S_w}{K_{HC}} + \frac{S_w}{K_B}\right)^{-1} \tag{4.14}$$

where S_w is an average of the water saturation (section 4.7) in the intervals of interest, corresponding to the Etive and Garn formations.

Before proceeding with the fluid substitution, a change of domain from bulk modulus to P-wave modulus was necessary. The reason for this was the lack of shear wave velocity

information; only four wells in the Norwegian Sea had S-wave velocity logs. Without shear wave velocity measurements, the shear modulus of the formations remains unknown, and, therefore, the bulk modulus of the saturated rock in situ cannot be estimated.

On the other hand, the saturated P-wave modulus of the formation, M_{sat}, in GPa, can be computed as:

$$M_{sat} = \rho_b V_P^2 \tag{4.15}$$

where ρ_b is the bulk density from the density log in g/cm^3, and V_P is the P-wave velocity from the acoustic log in km/s.

The P-wave modulus of the fluid mixture, M_{mix}, is the same as the bulk modulus of the fluid mixture, K_{mix}, given that there are only fluids involved (assuming zero shear modulus for the fluids). Similarly, the P-wave moduli of the individual fluids are the same as their respective bulk modulus, i.e. $M_B = K_B$, $M_G = K_G$, $M_{oil} = K_{oil}$.

For the P-wave modulus of quartz (matrix), M_0, a constant value of 95.4 GPa was used, assuming 2.65 g/cm^3 for the density and 6.0 km/s for the P-wave velocity.

With the values of P-wave modulus, Mavko et al. (1995) approximation of the Gassmann's relation (Equation 4.16) was used to perform the fluid substitution.

$$\frac{M_{sat}}{M_0 - M_{sat}} \approx \frac{M_{dry}}{M_0 - M_{dry}} + \frac{M_{fl}}{\phi(M_0 - M_{fl})} \tag{4.16}$$

Firstly, the P-wave modulus of the dry rock, M_{dry}, was computed as:

$$M_{dry} = \frac{M_0\left[\frac{M_{sat}}{M_0 - M_{sat}} - \frac{M_{fl}}{\phi(M_0 - M_{fl})}\right]}{\left[1 + \frac{M_{sat}}{M_0 - M_{sat}} - \frac{M_{fl}}{\phi(M_0 - M_{fl})}\right]} \tag{4.17}$$

where ϕ is the Formation's porosity calculated in section 4.4, and $M_{fl} = M_{mix}$. With this value of M_{dry}, the relationship in Equation 4.16 was used once again, this time to calculate the P-wave modulus of the rock for a 100% water saturated scenario, M_{sat}:

$$M_{sat} = \frac{M_0\left[\frac{M_{dry}}{M_0 - M_{dry}} + \frac{M_{fl}}{\phi(M_0 - M_{fl})}\right]}{\left[1 + \frac{M_{dry}}{M_0 - M_{dry}} + \frac{M_{fl}}{\phi(M_0 - M_{fl})}\right]} \tag{4.18}$$

where, in this case, M_{fl} is the P-wave modulus of the brine, M_B.

The P-wave velocity of the rock for a 100% water saturated scenario can then be calculated as:

$$V_{P_{Sw100}} = \sqrt{\frac{M_{sat_{Sw100}}}{\rho_{b_{Sw100}}}} \tag{4.19}$$

where $M_{sat\ Sw100}$ is the P-wave modulus of the rock when is 100% water saturated, calculated in Equation 4.18, and $\rho_{b\ Sw100}$ is computed as:

$$\rho_{b_{Sw100}} = (1-\phi)\rho_{ma} + \phi\rho_B \tag{4.20}$$

where ϕ is the Formation's porosity calculated in section 4.4, ρ_{ma} is the quartz density (2.65 g/cm^3) and ρ_B is the brine density calculated in section 4.8. Figure 4.8 summarizes the workflow for the fluid substitution.

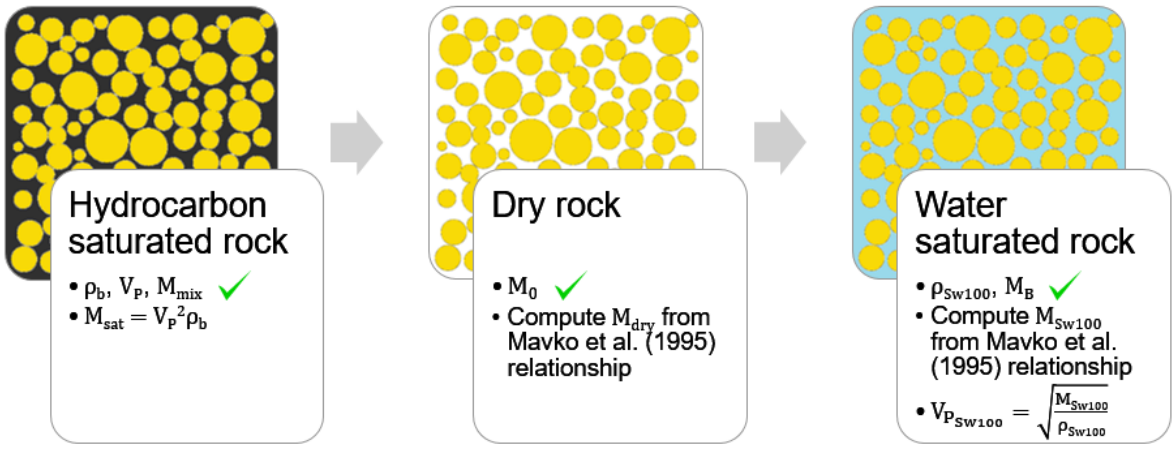

Figure 4.8. Fluid substitution workflow. The notation is the same as in the text.

Figure 4.9 shows a comparison between the P-wave velocity from the acoustic log and the P-wave velocity for a 100% water saturated scenario in one of the studied wells.

4.10 S-wave velocity estimation

From the previously calculated P-wave velocity at 100% water saturation, the S-wave velocity for the same scenario was estimated for the wells without S-wave velocity measurements. Greenberg and Castagna's relation (1992) was used:

$$V_S = \frac{1}{2}\left\{\left[\sum_{i=1}^{L} X_i \sum_{j=0}^{N_i} a_{ij} V_P^j\right] + \left[\sum_{i=1}^{L} X_i \left(\sum_{j=0}^{N_i} a_{ij} V_P^j\right)^{-1}\right]^{-1}\right\} \tag{4.21}$$

$$\sum_{i=1}^{L} X_i = 1$$

where L is the number of pure monomineralic lithologic constituents, X_i are the volume fractions of lithological constituents, N_i is the order of polynomial for constituent i, and a_{ij} are the empirical regression coefficients (Table 4.4) (Mavko et al., 2009). V_P and V_S are in km/s.

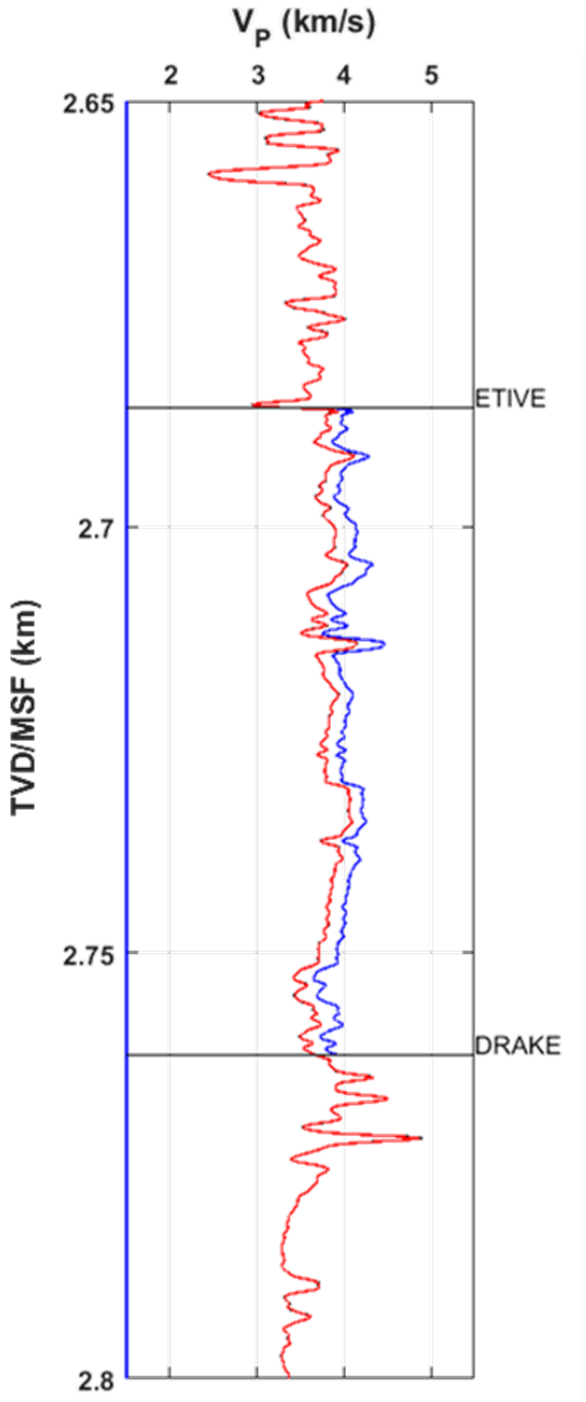

Figure 4.9. P-wave velocity from acoustic log (red) in well 30/3-4 and P-wave velocity for a 100% water saturated scenario after performing fluid substitution (blue) within the Etive Fm. The well originally contained oil. The bold blue line represents the P-wave velocity of water (1.5 km/s).

Table 4.4. Regression coefficients for the pure lithologies of interest, sandstone and shale. (From Mavko et al., 2009)

Lithology	a_{i2}	a_{i1}	a_{i0}
Sandstone	0	0.80416	-0.85588
Shale	0	0.76969	-0.86735

For the wells with S-wave velocity information and hydrocarbon content the approach was different. With the S-wave velocity computed from the logs (in km/s) and the bulk density from the density log readings (in g/cm^3), the shear modulus, μ_{sat} (in GPa), was calculated as:

$$\mu_{sat} = \rho_b V_S^2$$
$$\mu_{sat} = \mu_{dry} = \mu \tag{4.22}$$

Assuming that μ_{sat} remains the same regardless of fluid content, and calculating the bulk density of the rock for 100% water saturation as in Equation 4.20, the S-wave velocity for a 100% water saturated scenario can be computed as:

$$V_{S_{Sw100}} = \sqrt{\frac{\mu}{\rho_{b_{Sw100}}}} \tag{4.23}$$

Figure 4.10 shows a comparison of the S-wave velocity from log measurements and the S-wave velocity computed with Greenberg and Castagna's relation for a dry well (Figure 4.10.a)), and a comparison between the S-wave velocity from log measurements, the S-wave velocity calculated from Equation 4.23, and the S-wave velocity computed with Greenberg and Castagna's relation for a well originally containing hydrocarbons (Figure 4.10.b)).

4.11 Dry elastic moduli calculations – Dry bulk modulus and shear modulus

For all the wells, the dry shear modulus was calculated following Equation 4.22. If the S-wave velocity was obtained using Greenberg and Castagna's relation, the involved bulk density is the one corresponding to 100% water saturation (Equation 4.20).

The dry bulk modulus, K_{dry}, in GPa, was then computed following the relationship:

$$K_{dry} = M_{dry} - \frac{4}{3}\mu \tag{4.24}$$

where the dry P-wave modulus, M_{dry}, is the one calculated in section 4.9 (Equation 4.17).

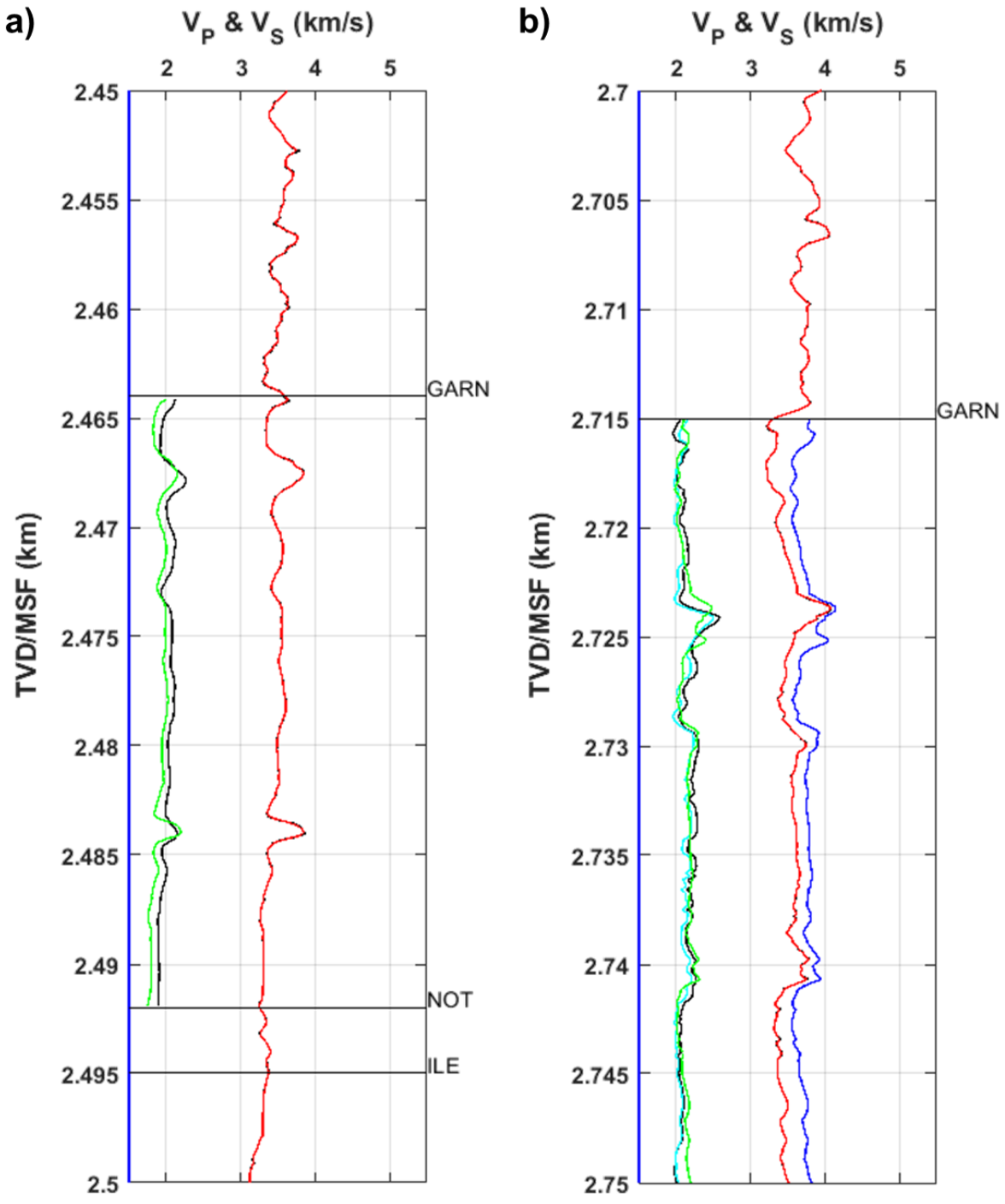

Figure 4.10. a) S-wave velocity from log (black) and S-wave velocity computed with Greenberg and Castagna's relation (green) for a dry well (6507/8-7) in the Norwegian Sea; the red curve is P-wave velocity from log. **b)** S-wave velocity from log (black), S-wave velocity calculated from Equation 4.23 (cyan), and S-wave velocity computed with Greenberg and Castagna's relation (green) for a well containing gas (6507/11-6) in the Norwegian Sea; the red curve is P-wave velocity from log and the blue curve is P-wave velocity at 100% water saturation. In both graphs the bold blue line represents the P-wave velocity of water (1.5 km/s).

4.12 Dry elastic moduli and velocities modeling

The dry elastic moduli were modeled by means of the friable-sand and contact-cement models presented in section 2.3, and then compared with the data obtained for the Etive and Garn sandstones. For both models, a constant coordination number, *n*, of 9 was used as a good representative for sandstones with 0.40 porosity. The bulk modulus and shear modulus of the mineral (quartz) were set to 36.9 and 44, respectively.

The choice of these two models is based on an attempt to model the diagenesis processes after deposition. As the friable-sand model assumes the porosity loss is only due to sorting deterioration, it can be used to describe the mechanical compaction domain, where grain packing can look very similar to the effect of sorting (Avseth et al., 2010). Similarly, as the contact-cement model assumes the porosity loss occurs only due to cementation, it is herein used to describe the chemical compaction domain. Figure 4.11 shows a schematic of the proposed modeling.

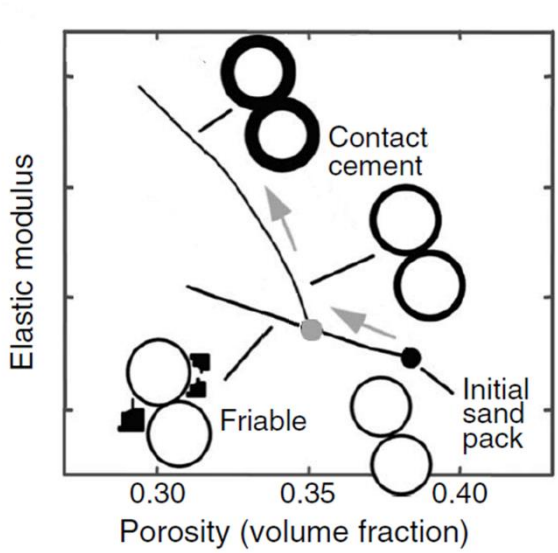

Figure 4.11. Schematic of the combination of the friable-sand and contact-cement models to follow the diagenetic processes after deposition. (Modified from Avseth et al., 2010)

The friable-sand model, however, is defined for a given effective stress (see Equations 2.8 and 2.9). To make the model consistent with the mechanical compaction process where the effective stress increases with burial depth, the friable-sand model was computed for stresses ranging from 1-25 MPa (with a step of 1 MPa), assuming these values are representative for the mechanical compaction domain. From the porosity modeling for the mechanical compaction (section 4.4.1), porosity and stress are related, and from this relation it was possible to identify the dry elastic moduli at certain porosity at certain stress. Figure 4.12 illustrates the model for mechanical compaction for the dry bulk modulus.

The friable-sand model was also tested with the Walton model for effective elastic moduli for smooth spheres (Walton, 1987). It results from replacing the effective elastic moduli from the Hertz-Mindlin model (Equations 2.8 and 2.9) with those defined by Walton for smooth spheres (1987). The reason for this is that the Hertz-Mindlin model defined in section 2.3.1 is related to infinite friction between the grains, whereas Walton model for smooth spheres is related to zero friction between the grains. The friction between the grains changes with effective stress, and is most likely to be closer to the zero friction limit at low stresses and closer to the infinite friction limit at higher stresses.

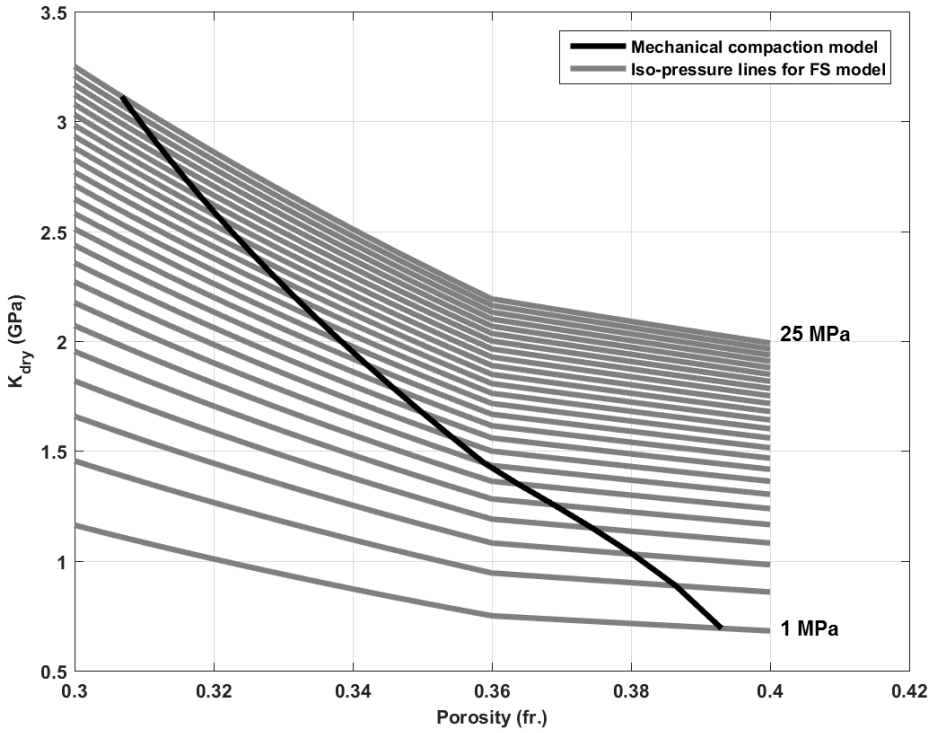

Figure 4.12. Mechanical compaction model for the dry bulk modulus (black) from the friable-sand model (gray). The friable-sand model is computed for stresses ranging from 1-25 MPa with a step of 1 MPa. FS = Friable-sand.

In the case of the contact-cement model, the model is originally defined to start at a porosity of 0.36. The model was firstly computed starting at 0.36 porosity until about 0.30 porosity. To take the model to start at the desired porosity (the porosity at the onset of quartz cementation), the values of stiffness moduli obtained previously were introduced in Hashin-Strikman lower bound relationship (Equations 2.10 and 2.11) as K_{HM} and μ_{HM}, while the critical porosity (ϕ_c) varied from 0.36 to about 0.30. Figure 4.13 illustrates these proceedings. From the lowest porosity reached with the modified contact-cement model, the corresponding values of elastic moduli were used constantly as K_{HM} and μ_{HM} in Hashin-Strikman lower bound relationship to continue the model until zero porosity.

Once K_{dry} and μ_{dry} were modeled, Gassmann fluid substitution relation was used to compute K_{sat} for a 100% water saturated scenario (similarly as in Equation 4.16 but replacing M with K), and the density at each porosity was also calculated for the same scenario (Equation 4.20), to model the P- and S-wave velocities and compare them with the data obtained in sections 4.9 and 4.10.

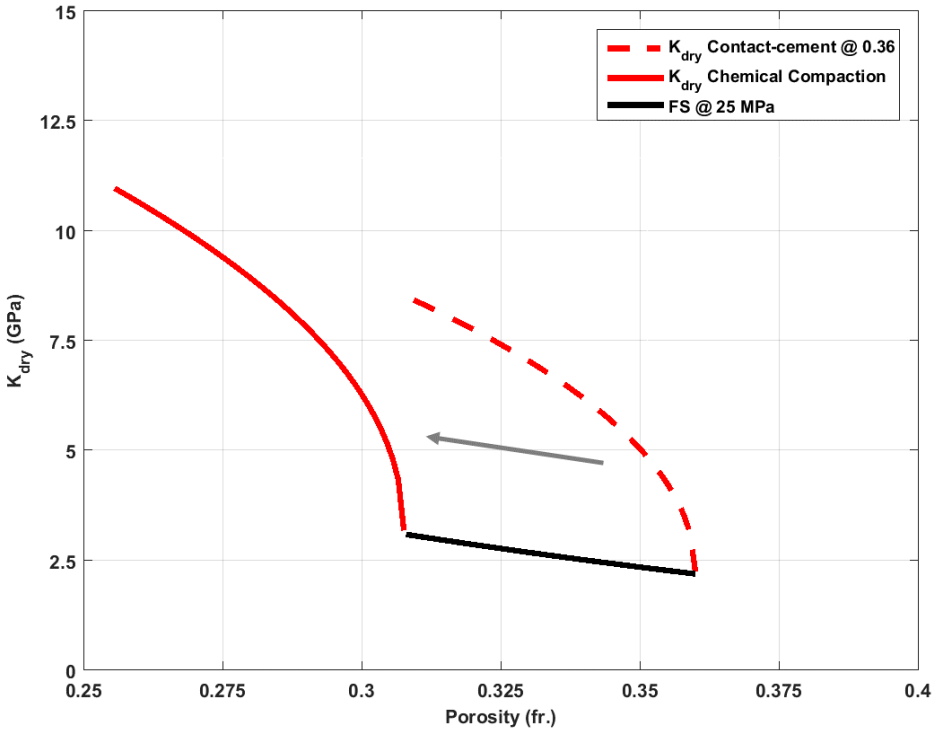

Figure 4.13. Modified contact-cement model to start at the onset of quartz cementation. The friable-sand model at 25 MPa is shown for reference.

From the porosity-depth relationships derived in section 4.4.1, the dry elastic moduli and the 100% water saturated velocities were converted to functions of depth instead of porosity.

CHAPTER 5 RESULTS

The results presented in this chapter are representative for the sandstones of the Etive and Garn formations with less than 5% of clay content, taken to a 100% water saturated scenario, according to the calculations presented in Chapter 4. For the graphs where different properties are plotted against depth, the depth is given as true vertical depth measured from sea floor.

The properties of the Etive sandstones are presented together with those of sandstones from the Utsira Fm. (Middle to Late Miocene in age) encountered in one of the studied wells (34/7-12), with the purpose of analyzing how the trends fit shallower sandstones.

5.1 Porosity-depth trends

As discussed in previous chapters, studying the porosity loss of a rock with burial depth is fundamental to understand the compaction processes, and how do these affect other physical properties of the rock. Figures 5.1 and 5.2 show the relationships between porosity and burial depth derived from the well data for the Etive and Garn sandstones, respectively, together with the porosity loss trends modeled in section 4.4.1.

For the Etive sandstones, the porosity loss modeling in the mechanical compaction domain shows good agreement with the shallower Utsira Fm. at about 0.8 km burial depth, however, it slightly under predicts the porosities for the Etive sandstones at around 1.5-2.0 km burial depth. At burial depths greater than 2 km, the porosity loss cannot be longer explained by the loss of the rock's IGV. At the start of the chemical compaction modeling (2 km burial depth) the porosity is near to 0.31. The chemical compaction modeling at burial depths greater than 2 km can explain the porosity loss in most of the sandstones within a range of different grain sizes representative for the Etive Fm. For three wells, however, the porosities of the Etive Fm. are not explained by the chemical compaction models. At about 2.7 km burial depth, the Etive sandstones encountered in well 30/3-4 have an anomalous higher temperature than those in their surroundings, and lower porosities than those predicted by the models. For two wells at around 4.1 km burial depth (34/10-23 and 34/11-4) the sandstones porosities are in fact higher than the ones predicted by the models.

In the case of the Garn sandstones, the porosity loss modeling in the mechanical compaction domain slightly under predicts the porosity in sandstones about 1.7 km burial depth encountered in well 6507/12-3, similarly as for the Etive sandstones at comparable depths. However, the only point representative of Garn Fm. with less than 5% clay in well 6507/8-6, at about the same depth as Garn Fm. in well 6507/12-3, has a significant lower porosity (0.26) than the one predicted by the model (0.30) at the same depth. At burial depths greater than 2 km, the porosity

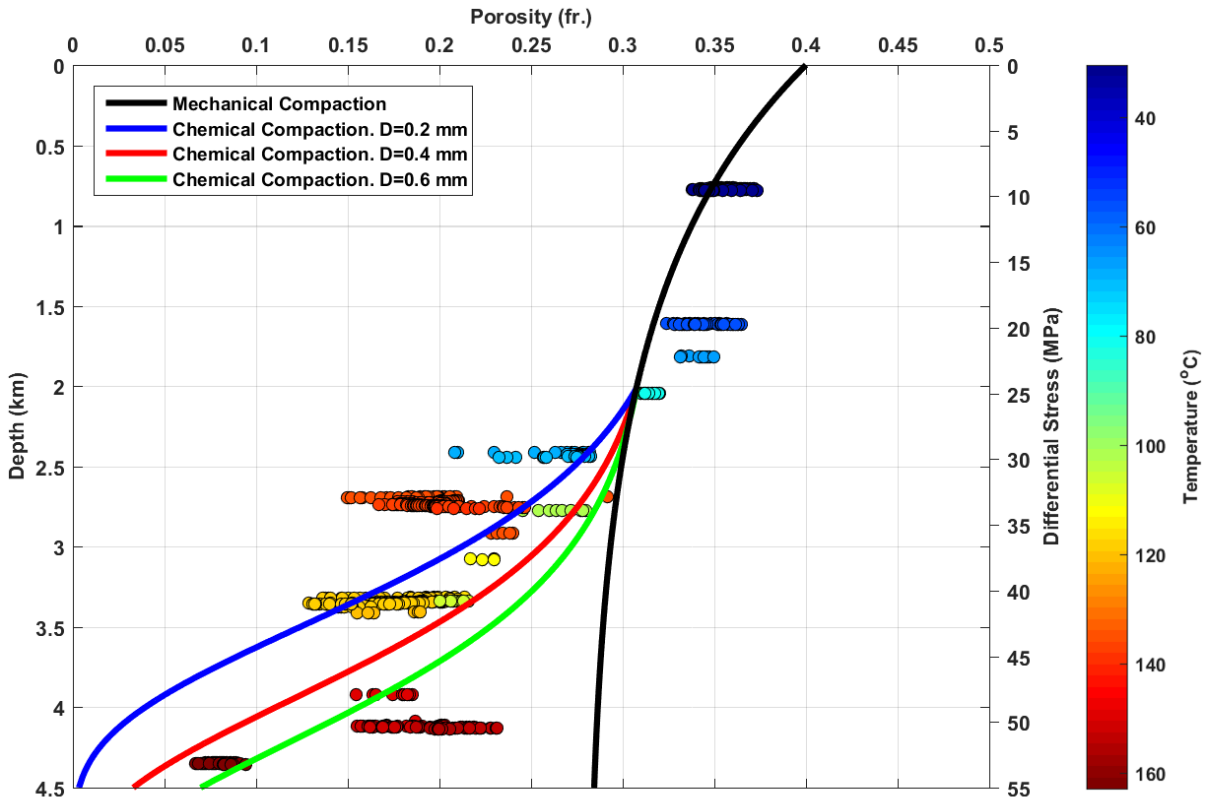

Figure 5.1. Porosity-depth trends in the mechanical and chemical domains for the sandstones of the Etive Fm. color-coded by Formation temperature. *D* = grain size.

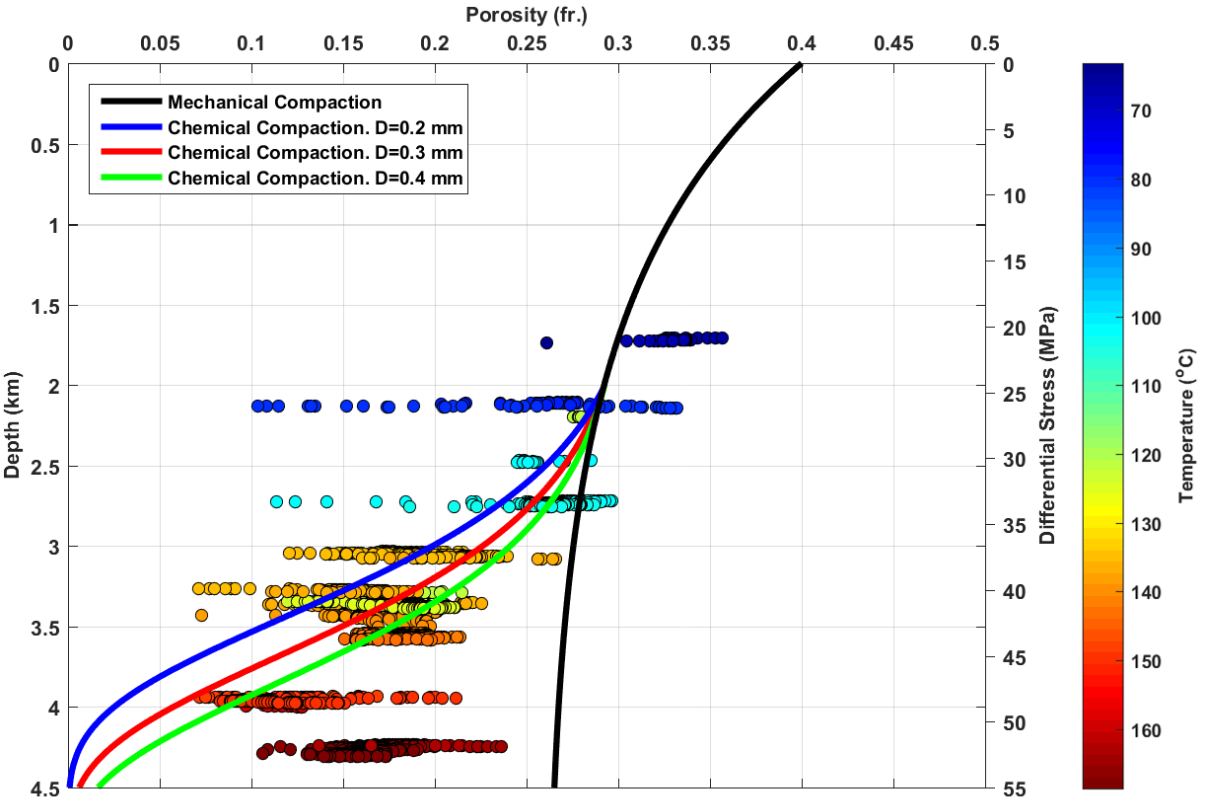

Figure 5.2. Porosity-depth trends in the mechanical and chemical domains for the sandstones of the Garn Fm. color-coded by Formation temperature. *D* = grain size.

loss is not explained by the modeling for the mechanical compaction domain (IGV loss), however, some points at depths between 2.1-2.7 km seem to maintain high porosities. At the start of the chemical compaction modeling (2 km burial depth) the porosity is about 0.29. The chemical compaction modeling at burial depths greater than 2 km can explain the porosity loss in most of the sandstones within a range of different grain sizes representative for the Garn Fm. Similarly as for the Etive Fm., the porosities of the Garn Fm. encountered at depths between 4.0-4.3 km are considerably higher than the ones predicted by the models. It is also noticeable that at depths corresponding to the chemical compaction domain, the porosities of the Garn Fm. encountered in one same well can vary considerably. In relation to this, the Garn sandstones in wells 6507/11-3 (~2.1 km burial depth) and 6507/11-6 (~2.7 km burial depth) appear to have porosities ranging from 0.1-0.3.

Appendix B shows the median values of porosity versus burial depth for the sandstones encountered in each well, together with the models presented in Figures 5.1 and 5.2.

Figure 5.3 shows the density values obtained for a 100% water saturated scenario in the Etive and Garn formations, together with density-depth trends derived from the porosity trends. The behavior of the curves is consistent with those presented in Figures 5.1 and 5.2.

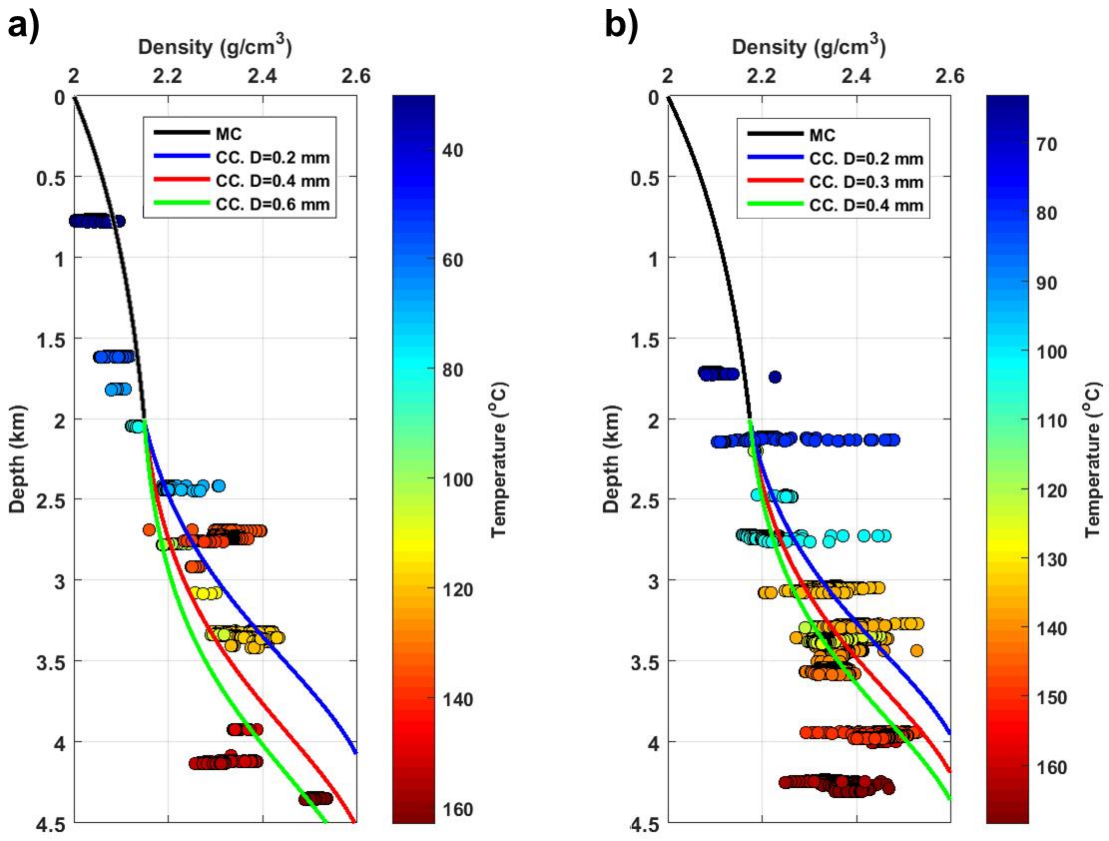

Figure 5.3. Density-depth trends for the Etive Fm. (Figure 5.3.a)) and for the Garn Fm. (Figure 5.3.b)). MC = mechanical compaction, CC = chemical compaction.

5.2 Dry elastic moduli- and velocities-porosity trends

The dry elastic moduli (K_{dry} and μ_{dry}) calculated for both the Etive and Garn formations in sections 4.10 and 4.11 are presented together with the models for dry elastic moduli-porosity discussed in section 4.12. Figures 5.4 and 5.5 correspond to the data for the Etive Fm. and Figures 5.6 and 5.7 correspond to the data for the Garn Fm.

The mechanical compaction curves, both for infinite friction and zero friction, over predict the dry bulk modulus for the Utsira Fm. and under predict the dry bulk moduli for the shallower Etive sandstones (Figure 5.6). In the case of the dry shear modulus, however, the zero friction curve follows the values of the Utsira Fm. and the infinite friction limit is closer to explain the shallower Etive sandstones, although is still under predicting the values of μ_{dry} (Figure 5.5). The results for the Garn Fm. in the mechanical domain are similar to those of the Etive Fm.; K_{dry} is significantly under predicted by the models while μ_{dry} modeled with infinite friction is closer to the data values (Figures 5.6 and 5.7).

The chemical compaction curve continues from the mechanical compaction curve for the infinite friction model, arguing that at the onset of quartz cementation the behavior of the rock will be closer to the infinite friction limit than to the zero friction limit. The quartz cement is assumed to increase along the chemical compaction curve.

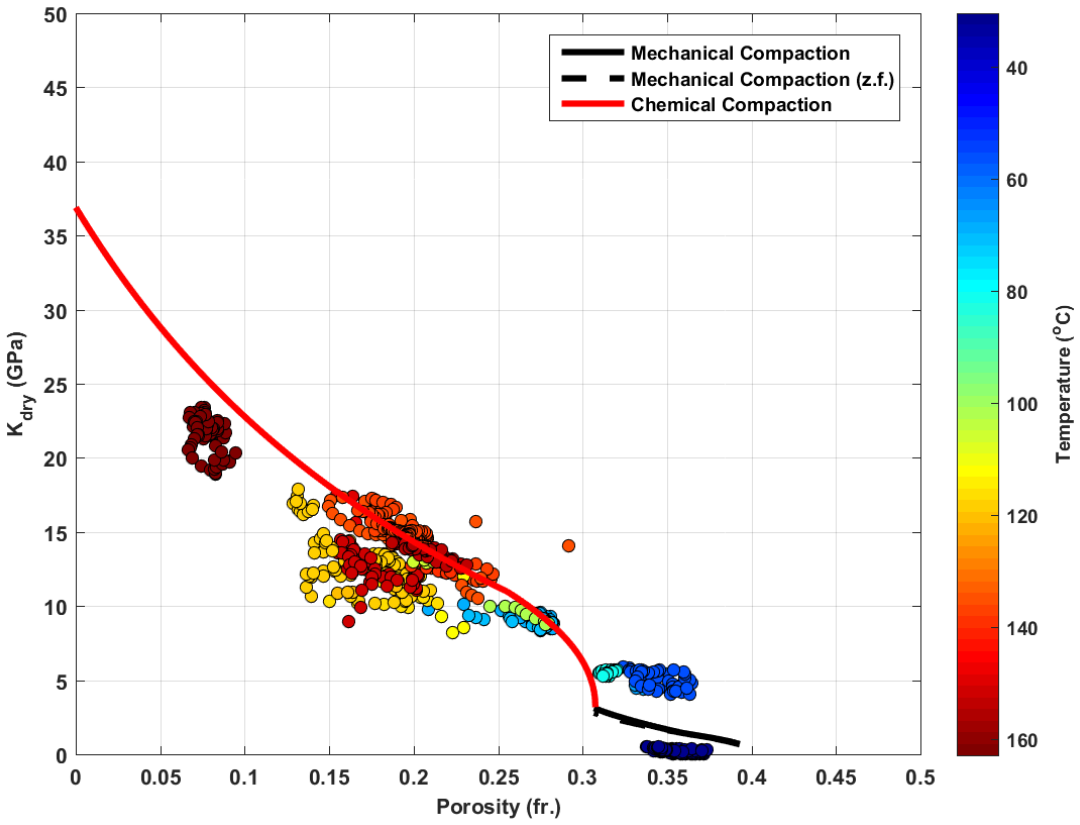

Figure 5.4. Dry bulk modulus versus porosity for the Etive Fm. with compaction models. The data points with the lowest K_{dry} values correspond to the Utsira Fm. (z.f. = zero friction).

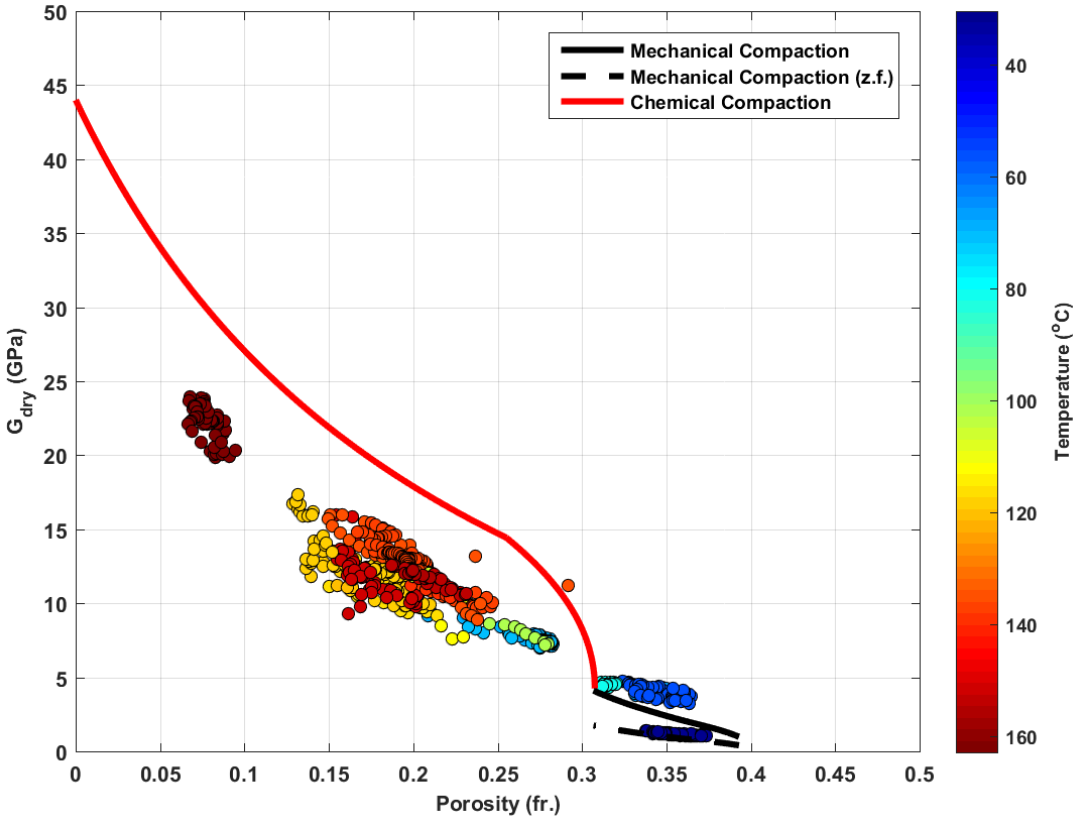

Figure 5.5. Dry shear modulus versus porosity for the Etive Fm. with compaction models. The data points with the lowest μ_{dry} values correspond to the Utsira Fm. (z.f. = zero friction; $G_{dry} = \mu_{dry}$).

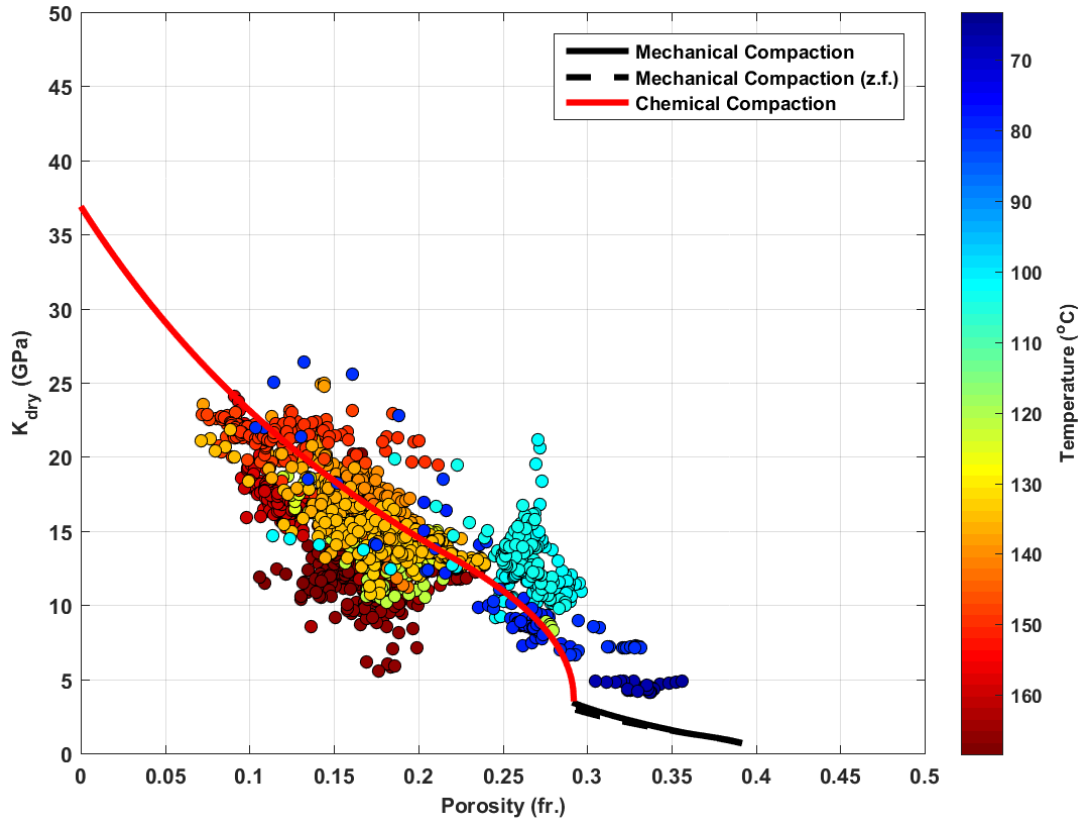

Figure 5.6. Dry bulk modulus versus porosity for the Garn Fm. with compaction models. (z.f. = zero friction).

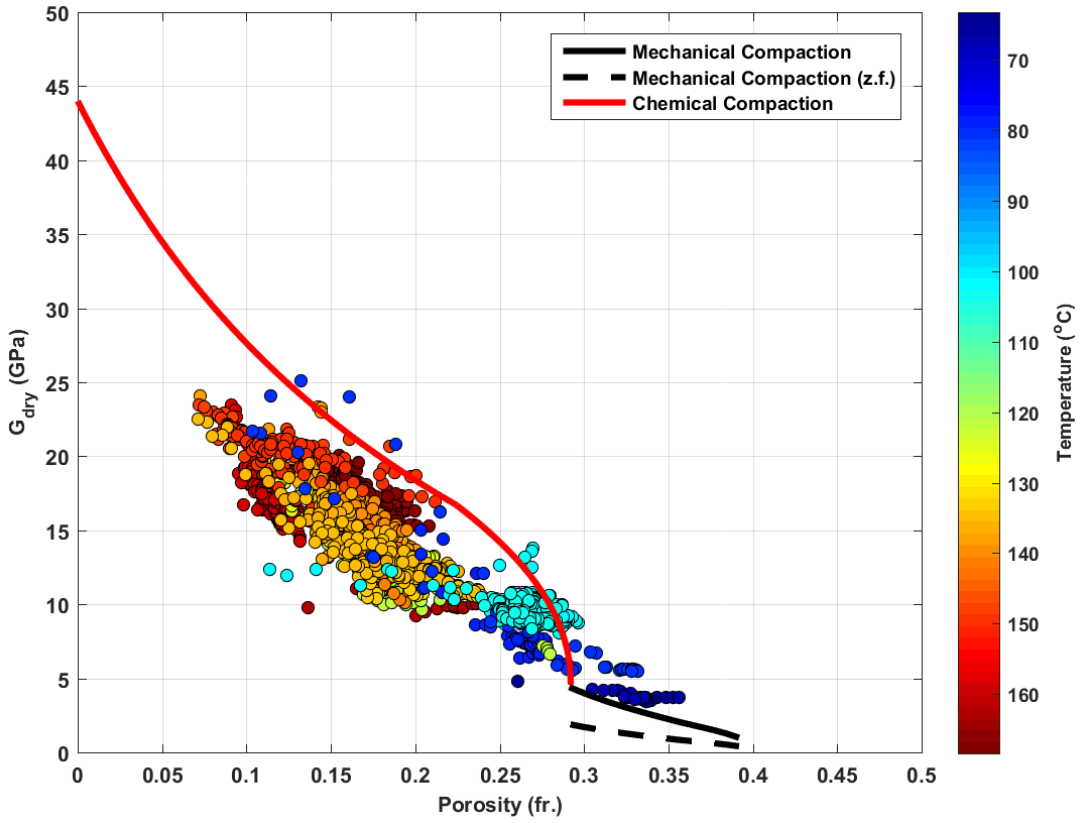

Figure 5.7. Dry shear modulus versus porosity for the Garn Fm. with compaction models. (z.f. = zero friction; $G_{dry} = \mu_{dry}$).

The chemical compaction curve follows the increasing bulk modulus with reducing porosity trend from the data (for both the Etive and Garn formations), although it mostly over predicts the values, especially for the hotter (and deeper) sandstones in both formations (Figures 5.4 and 5.6). From the data, it can also be observed that same values of porosity can result in different values of bulk modulus, and these differences are greater in the Garn Fm.

In the case of the dry shear modulus, for both the Etive and Garn sandstones, the model significantly over predicts the values, especially for the Etive Fm. (Figures 5.5 and 5.7). What is also noticeable from the data points, is that the values of dry shear modulus at a given porosity vary less than those of the dry bulk modulus.

Figures 5.8 to 5.11 show the correspondent trends for P- and S- wave velocities for the Etive and Garn formations at 100% water saturation as a function of porosity. In the mechanical compaction domain, the data of the Utsira Fm. mostly aligns with the zero friction model (Figures 5.8 and 5.9), while the shallower Etive and Garn sandstones are still not explained by the models. In the chemical compaction domain, both V_P and V_S models over predict the data, as expected from the over predictions in K_{dry} and μ_{dry}.

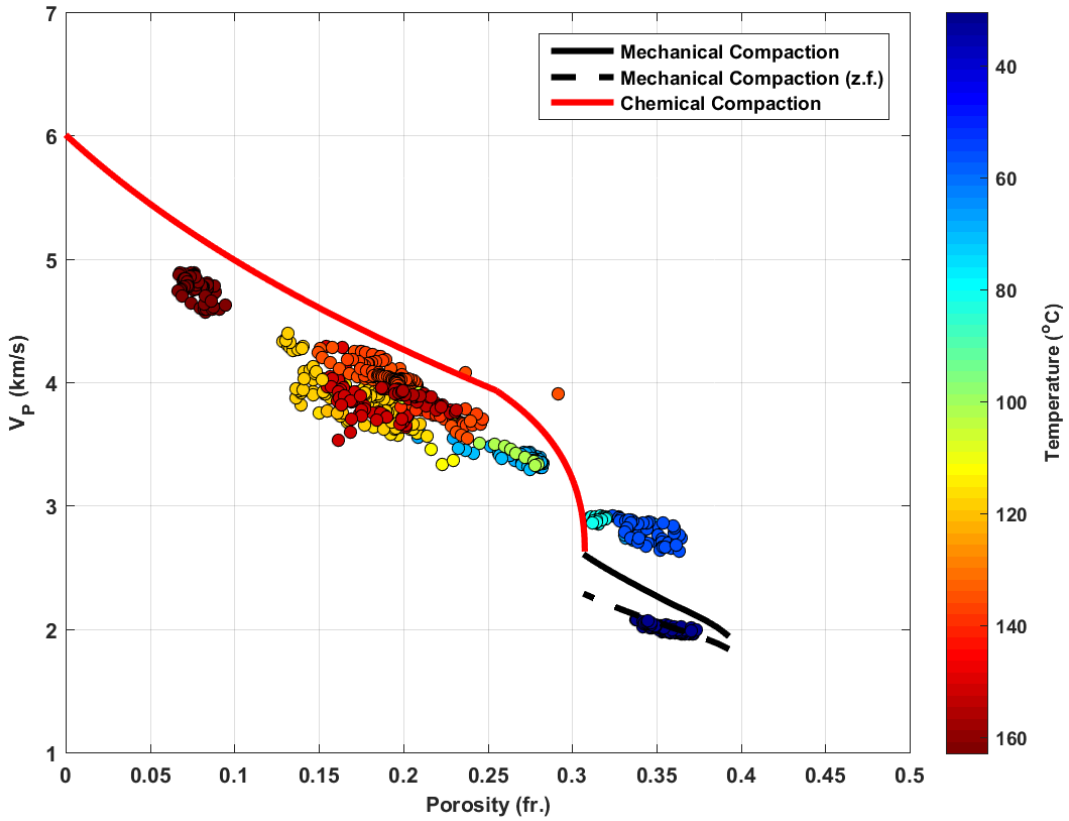

Figure 5.8. P-wave velocity at 100% water saturation versus porosity for the Etive Fm. with compaction models. The data points with the lowest V_P values correspond to the Utsira Fm. (z.f. = zero friction).

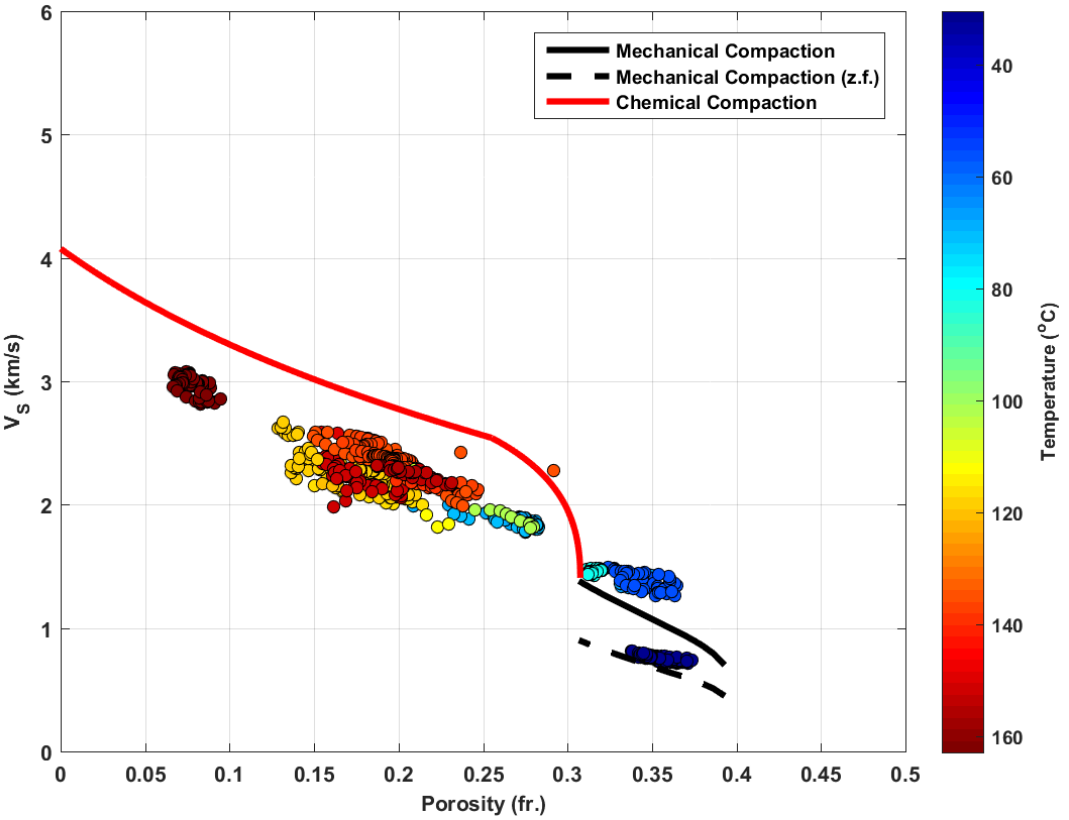

Figure 5.9. S-wave velocity at 100% water saturation versus porosity for the Etive Fm. with compaction models. The data points with the lowest V_S values correspond to the Utsira Fm. (z.f. = zero friction).

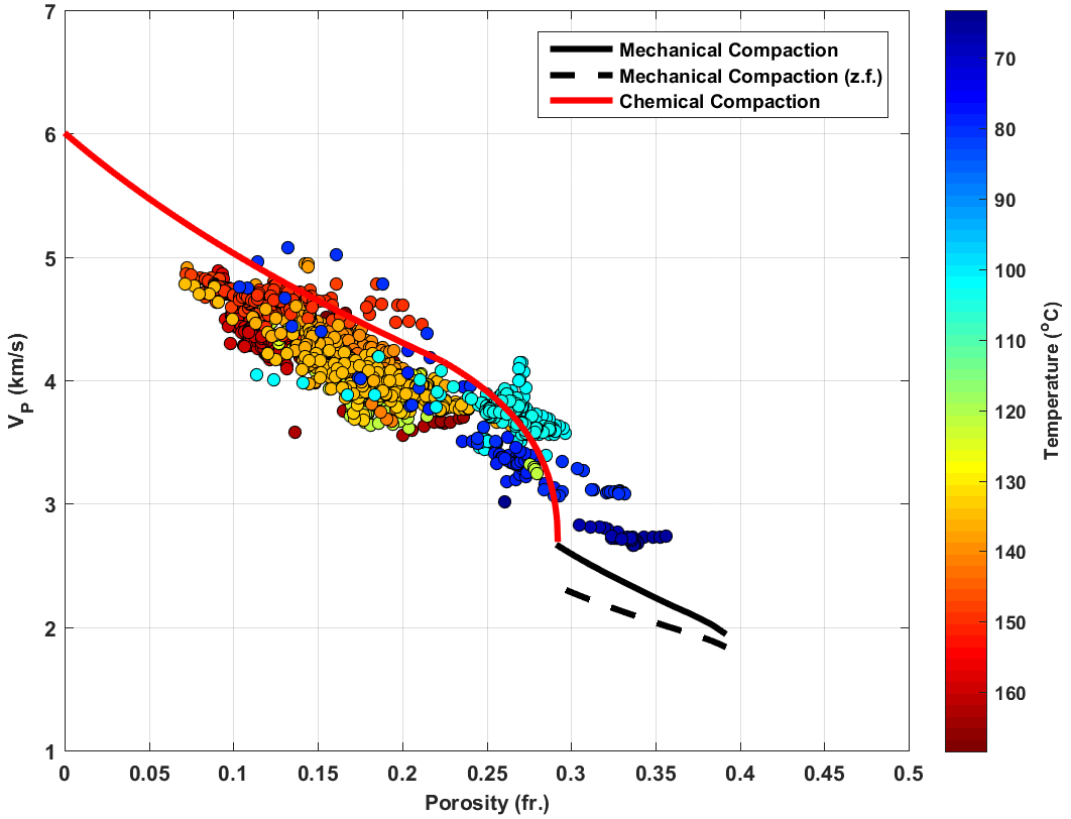

Figure 5.10. P-wave velocity at 100% water saturation versus porosity for the Garn Fm. with compaction models. (z.f. = zero friction).

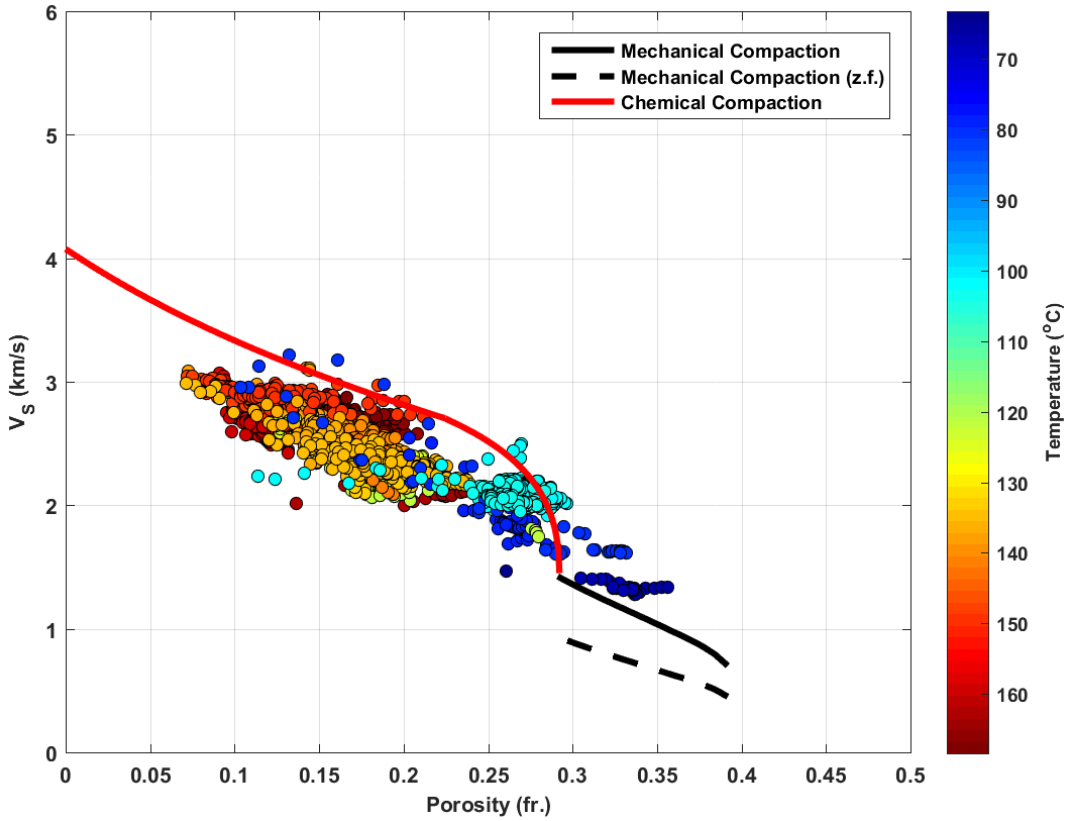

Figure 5.11. S-wave velocity at 100% water saturation versus porosity for the Garn Fm. with compaction models. (z.f. = zero friction).

5.3 Dry elastic moduli- and velocities-depth trends

The models for dry elastic moduli and velocities presented in the previous section were converted to a depth domain from the relationships porosity-depth shown in section 5.1. Figures 5.12 to 5.15 show the data for dry elastic moduli and velocities as a function of burial depth for the Etive and Garn formations, together with the derived models for mechanical and chemical compaction. In this case, the data is color-coded with porosity to illustrate better the changes in these rock physical properties for sandstones encountered in a same well, but with varying porosity.

The mechanical compaction trend is only shown for the infinite friction model. From this, it can be observed that the model over predicts the properties for the Utsira Fm. (Figures 5.12 and 5.13). For both the Etive and Garn formations, the mechanical model under predicts the values of K_{dry} and V_P, but it does explain the data for μ_{dry} and V_S.

In the chemical compaction domain, the models can fairly explain the dry bulk modulus data for both Etive and Garn sandstones up to about 3.5 km burial depth, at larger depths the models greatly over predict the data. In the case of the dry shear modulus, the models mainly over predict the data, with the over prediction increasing with depth. From these results for elastic moduli, it is expected that the velocity models will mostly over predict the data, with the over prediction being larger for V_S than for V_P, as seen in Figures 5.13 and 5.15.

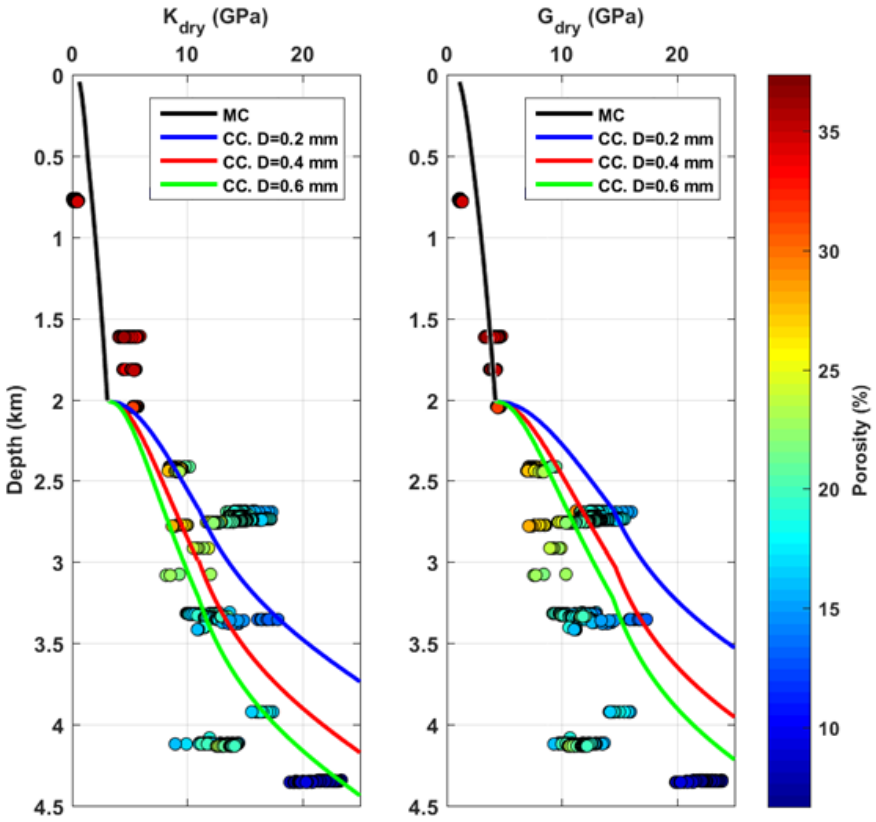

Figure 5.12. Dry elastic moduli versus depth for the Etive Fm. with compaction models. The data is color-coded with porosity. (MC = mechanical compaction, CC = chemical compaction; *D* = grain size).

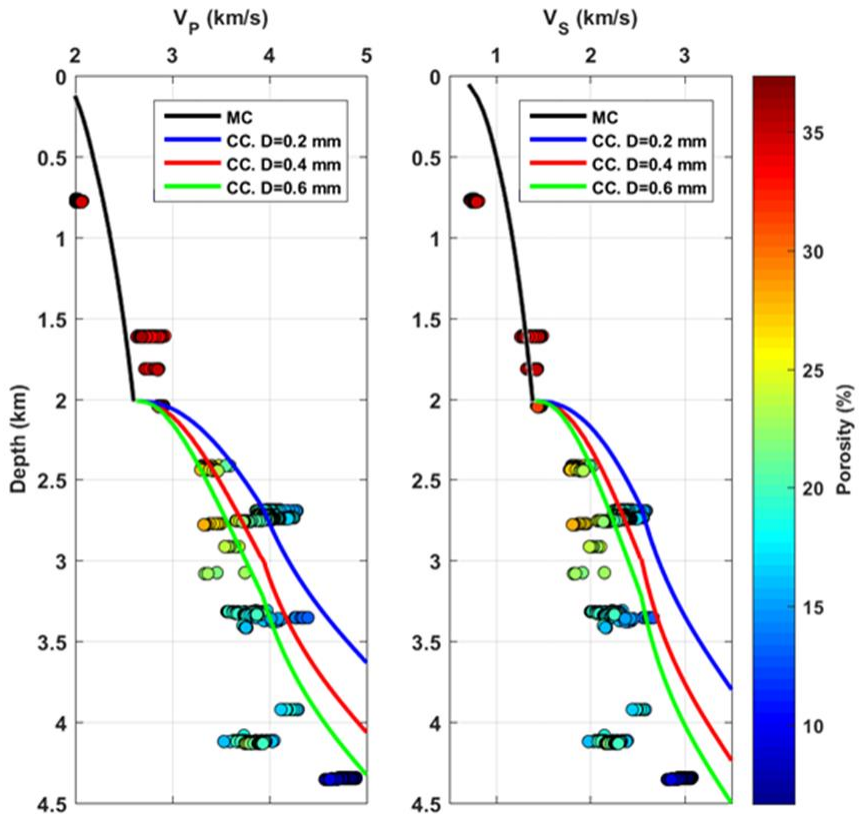

Figure 5.13. P- and S- wave velocities (S_w=100%) versus depth for the Etive Fm. with compaction models. The data is color-coded with porosity. (MC = mechanical compaction, CC = chemical compaction; *D* = grain size).

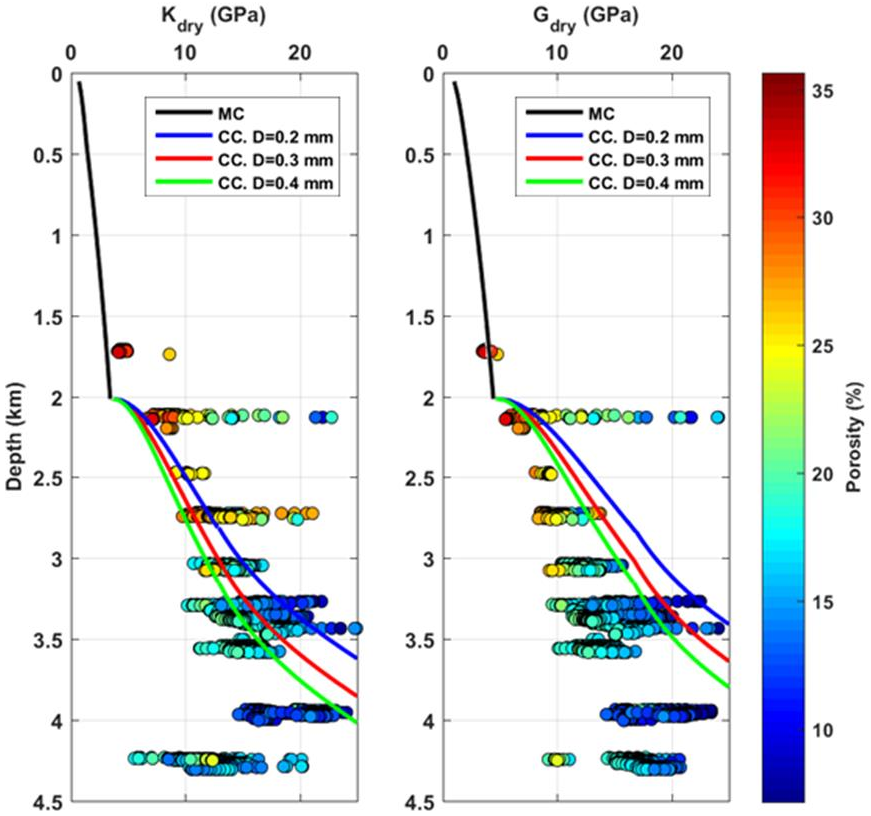

Figure 5.14. Dry elastic moduli versus depth for the Garn Fm. with compaction models. The data is color-coded with porosity. (MC = mechanical compaction, CC = chemical compaction; *D* = grain size).

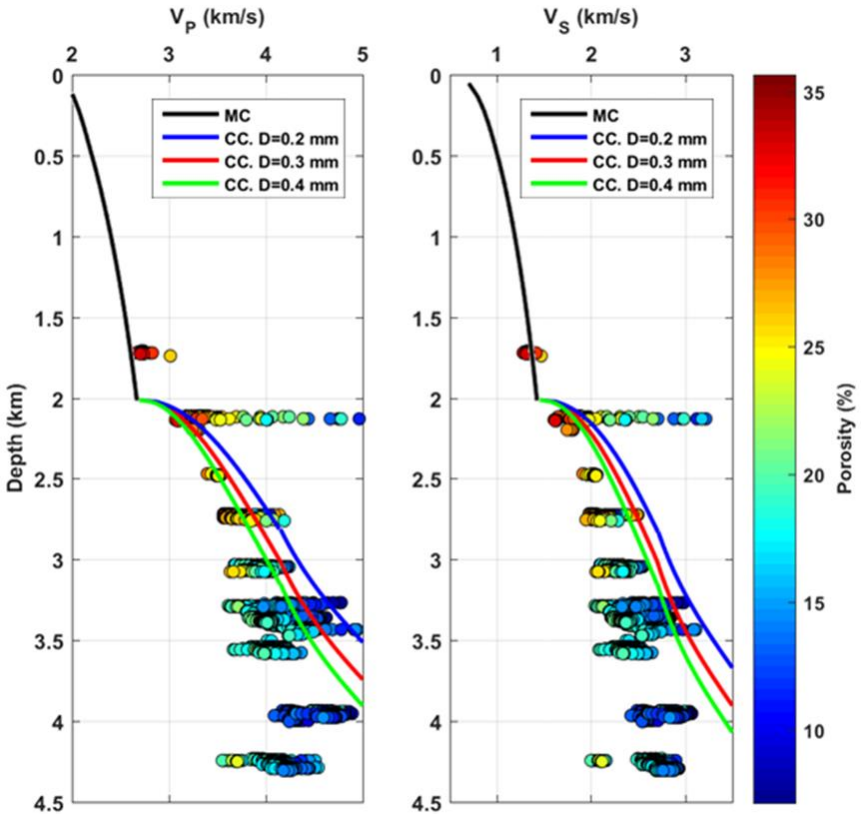

Figure 5.15. P- and S- wave velocities (S_w=100%) versus depth for the Garn Fm. with compaction models. The data is color-coded with porosity. (MC = mechanical compaction, CC = chemical compaction; *D* = grain size).

Appendix C shows the median values (for each well) of all the physical properties presented in this Chapter versus burial depth. For each property, the values of the Etive Fm. and the Garn Fm. are presented together. Linear regressions for each Formation are included.

CHAPTER 6 DISCUSSION

6.1 Porosity modeling

The porosity modeling in the mechanical compaction domain is mainly controlled by the depositional porosity and the final intergranular volume. The under prediction in porosity for sandstones shallower than 2 km burial depth can be a result of variations in these values. Figure 6.1 shows a comparison between two different schemes of IGV-Depth modeling for the Etive sandstones, together with IGV data from Marcussen et al. (2010). The solid line corresponds to the same model presented in this study (section 4.4.1 and Figure 5.1), while the dashed line represents a model with depositional porosity of 0.45 and final intergranular volume of 0.29. The later shows a better agreement with the IGV measurements, possibly indicating that the Etive Fm. has depositional porosities greater than 0.4, which is also supported by the measurements indicating IGV values of about 0.4 at burial depths around 2 km. Although IGV values as low as 0.28 had been measured, the sandstones show high IGV values (0.3-0.4) at burial depths around 4 km.

A similar reasoning can explain the under predicted porosity for the Garn sandstones encountered in well 6507/12-3. In the case of well 6507/8-6, where the sandstone porosity is considerably lower than the modeled one, only one point might not be representative for the entire Garn Formation. If it does, however, correspond to the true Formation porosity, the low porosity can be a result of carbonate cementation.

Another reason for the high porosity values at around 1.5-2.0 km burial depth both in the Etive and Garn formations can be overpressure, where high pore pressure results in higher porosities. Wells 34/10-3 and 34/10-9 in the North Sea are drilled in the Gullfaks field, which is known to have overpressured areas (NPD's FactPages: Gullfaks field). The pressure prediction report for well 34/10-3 stated a pore pressure gradient higher than the hydrostatic gradient at the top of the Brent Group. The completion report for well 34/10-9 indicated that the pore pressure was close to the formation integrity. For well 6507/12-3 in the Norwegian Sea normal values of formation pressure are stated.

In the chemical compaction domain, the porosity loss is a consequence of quartz cementation, and the amount of cemented quartz is greatly controlled by grain size, clay coating and temperature history. From Figures 5.1 and 5.2 it is clear that varying grain sizes result in different porosities, and therefore, given the model's definition, in varying amounts of cemented quartz; a difference of 0.1 mm in grain size can result in a difference up to 0.05 (fraction) of quartz cement. Smaller grain sizes lead to greater quartz surface areas and, therefore, higher amounts of quartz cement are precipitated.

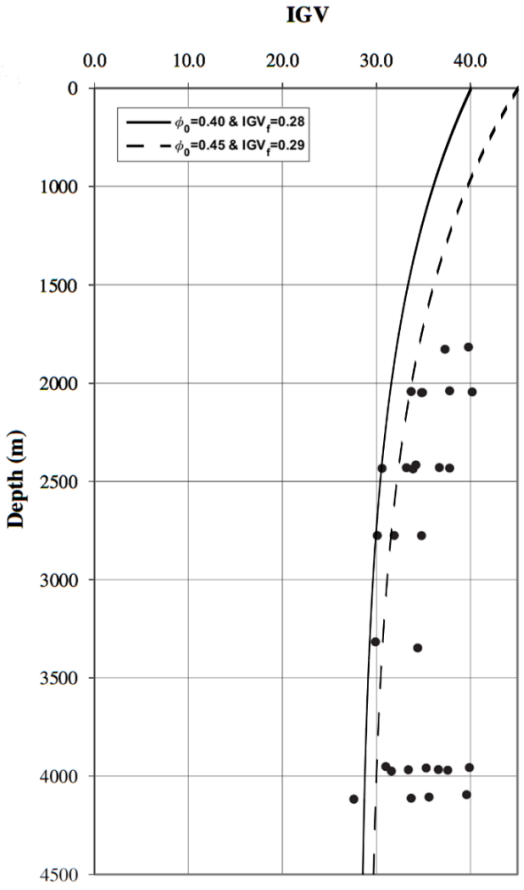

Figure 6.1. IGV versus depth models together with IGV measurements for the Etive Fm. from Marcussen et al. (2010). Higher depositional porosities and final intergranular volumes show better agreement with the data. (Modified from Marcussen et al. (2010))

Figure 6.2 shows the amounts of quartz cement in the Etive sandstones quantified by Marcussen et al. (2010) from several samples in seven different wells (which are also analyzed in this study), together with the quartz cement trends corresponding to the porosity modeling shown in Chapter 5. Marcussen et al. (2010) report small values of quartz cement (~0.07) in well 34/10-3 at about 1.82 km burial depth. This can explain the mismatch between the models and the data for the shallower wells (34/10-3 and 34/7-12), and for some points of wells 30/6-10 and 34/10-17. In the two deepest wells (30/2-2 and 34/10-23), however, the amounts of quartz cement are mostly over predicted, which is in consistency with the under prediction in porosity (Figure 5.1). From the quartz cement quantification, it can also be observed that sandstones encountered in a same well can have different amounts of quartz cement, which can explain the varying porosity values in sandstones that have suffered chemical compaction (see the greater spread in porosity values for the Etive sandstones buried deeper than 2 km in Figure 5.1, and also for the Garn sandstones in Figure 5.2).

Quartz cement quantification for the Garn sandstones encountered in four of the studied wells was available from Ehrenberg (1990). Figure 6.3 shows the values documented by Ehrenberg together with the quartz cement trends corresponding to the porosity modeling in the Garn Fm.

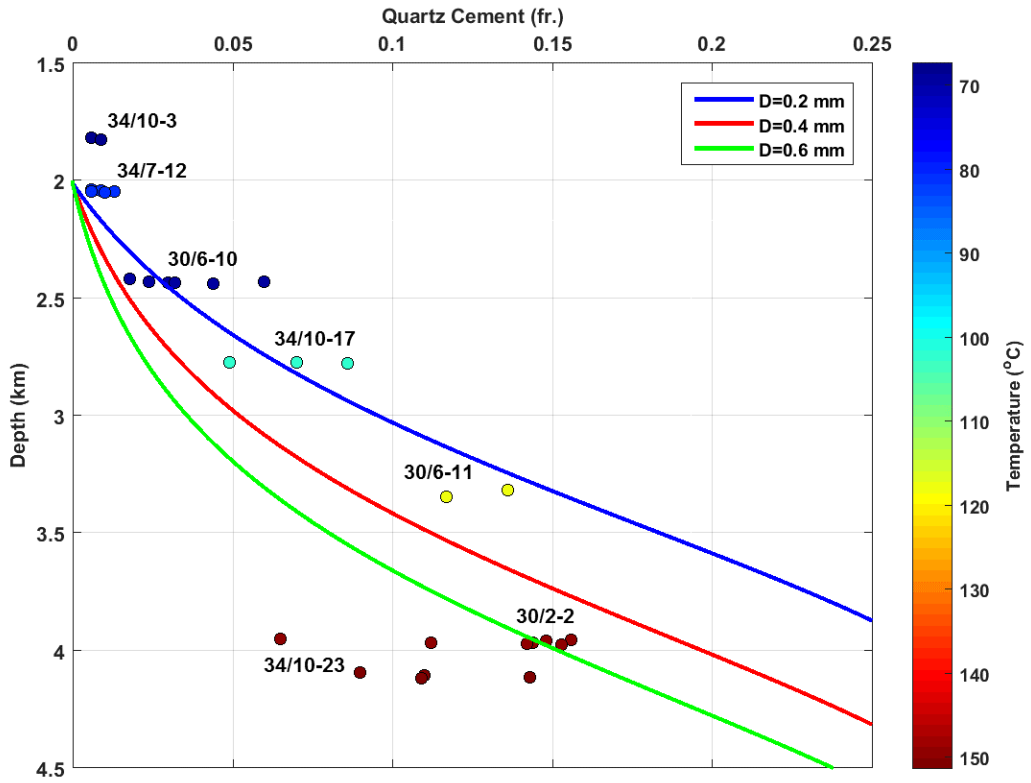

Figure 6.2. Quartz cement quantification for Etive sandstones encountered in seven wells (from Marcussen et al. (2010)) together with quartz cement models. Observe how for well 30/2-2 the amount of quartz cement varies between 0.07-0.15. *D* = grain size.

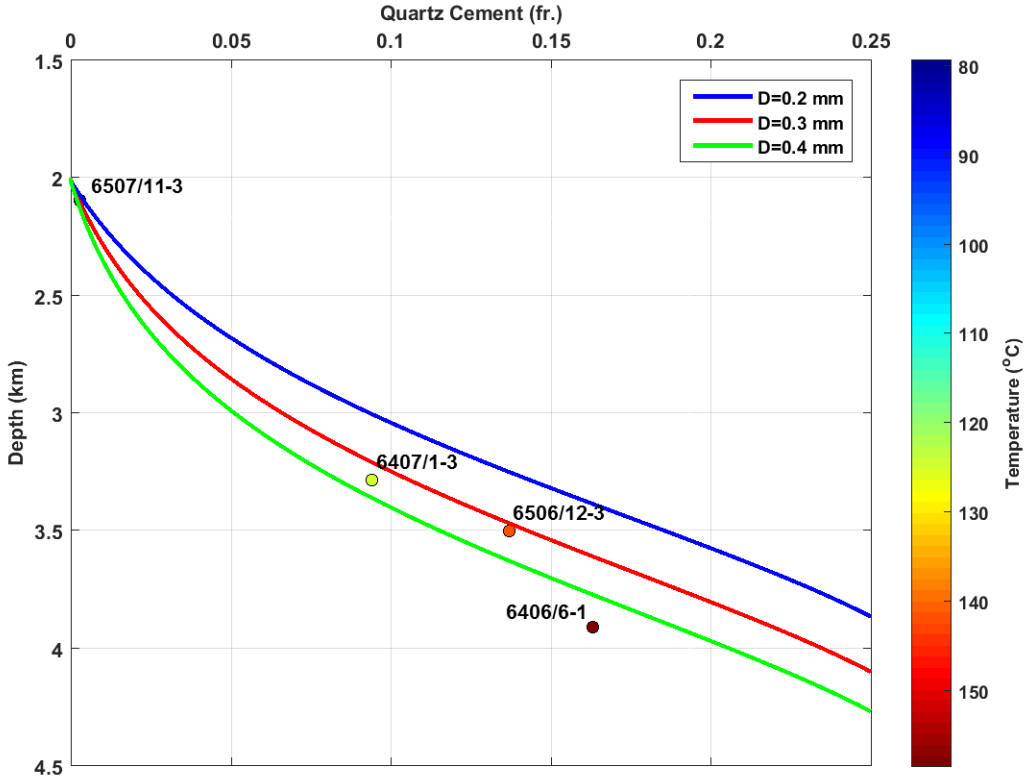

Figure 6.3. Quartz cement quantification for Garn sandstones encountered in four wells (from Ehrenberg (1990)) together with quartz cement models. *D* = grain size.

Although Ehrenberg presented averaged values of quartz cement, they can be explained by the models, except for the deepest well (6406/6-1), where the amount of quartz cement is over predicted, similarly as for the Etive Fm. in wells at around 4 km burial depth. From Ehrenberg's study (1990), there were no wells with quantified quartz cement in the Garn Fm. at burial depths shallower than 2 km, therefore, it is difficult to say anything about quartz cementation occurring at these depths. Since the values of quartz cement are averaged, it is an unknown if for the sandstones encountered in a same well the amount of quartz cement varies considerably, however, this would explain the great variations in porosity for the Garn sandstones that suffered chemical compaction (Figure 5.2). The larger variations in porosity values of the Garn Fm. at same depths, in comparison with the Etive Fm., is also an indicative that the Garn Fm. is less well sorted than the Etive Fm.

As seen from Figures 6.2 and 6.3, grain size is a variable there is control on provided values that are representative for the formations. Clay coating and temperature history, however, have higher uncertainties, especially when constant values of each variable are set to explain sandstones encountered in different wells, and therefore, that have been deposited in different areas. In the modeling presented in this study, the rate of porosity loss (or quartz cementation) for the Garn Fm. is higher than the one for the Etive Fm. because the estimated temperature increase rate in the Garn Fm. is also higher than the one for the Etive Fm. (section 4.4.1). Although for the Etive Fm., the models significantly over predict the porosity for the sandstones encountered in well 30/3-4, which might be a result of its anomalous high present day temperature, indicating a possibly higher temperature increase rate for these sandstones and therefore a higher quartz cementation rate.

For both the Etive and the Garn formations, the sandstones encountered in the deeper wells seem to preserve their porosity (with the exception of well 34/8-7 in the North Sea). All these sandstones have present day temperatures greater than 140°C, therefore, the preservation of porosity is not likely to be a result of lower temperature increase rates. Nevertheless, higher amounts of clay coating inhibit quartz cementation, and can possibly explain the observations. At Haltenbanken, the Garn Fm. has abundant chlorite coatings and also illite coatings (Ehrenberg, 1993, Storvoll et al., 2002). Similarly, Walderhaug (2000) documented abundant clay coatings in the sandstones from the Brent Group in the northern North Sea.

Another reason for porosities higher than expected at these great burial depths might be overpressure. Ehrenberg (1990) concluded that overpressure seemed to be favorable for porosity preservation in Garn sandstones below 3 km burial depth. The two deepest wells that encountered Garn sandstones studied herein (6406/2-7 and 6406/2-3) reported very high pore pressures in the Garn Fm., reaching gradients of about 1.97-1.99 g/cm^3 in equivalent mud weight (NPD's FactPages), and their median porosity values are about 0.22 and 0.16 (Appendix B). In the case of the Etive sandstones, well 34/8-7 (deepest well encountering the Etive Fm. in this study) reported 1.82 g/cm^3 for the drilling mud weight at the Etive Fm. interval (NPD's FactPages), indicative of significant overpressure. For wells 34/10-23 and 34/11-4 (Valemon

field) at about 4.1 km burial depth, the reports indicate mud weights of about 2.00 g/cm^3 for the Etive Fm. interval (NPD's FactPages), corresponding to even higher overpressures. The Etive Fm. in wells 34/10-23 and 34/11-4 is about 200 m shallower than the Etive Fm. in well 34/8-7, yet for the first wells the porosity values are significantly higher than those in the later one (Figures 5.1 and B.1).

There were no available measurements of quartz cement volume in the Etive and Garn sandstones encountered in the deepest wells (34/8-7, and 6406/2-3 and 6406/2-7, respectively) to compare them with the quantifications in slightly shallower wells (34/10-23 and 6406/6-1, for example), however, based on the previous arguments, greater amounts of clay coatings and higher pore pressures could together explain the preservation of porosity at large burial depths (> 4 km burial depth).

6.2 Dry bulk moduli and velocities modeling

The model's under prediction of dry bulk modulus and P-wave velocity in the mechanical domain, for both the shallower Etive and Garn sandstones, is most likely a result of these sandstones already having a minor amount of quartz cement stiffening the rock. From Marcussen et al. (2010) it is known that the Etive Fm. in wells 34/10-3 and 34/7-12 (at present day temperatures of about 60-80°C) has small amounts of quartz cement (Figure 6.2). Although there was no available information about quartz cement in the shallower Garn sandstones (in wells 6507/12-3 and 6507/8-6), small amounts of quartz cement would also explain the under prediction in K_{dry} and V_P.

From the dry elastic moduli-porosity graphs, it can be observed that the dry shear modulus model has a steeper slope than the dry bulk modulus model, which indicates that μ_{dry} increases more rapidly with increasing stress than K_{dry}. This steeper slope also explains why the values of μ_{dry}, and subsequently V_S, are less under predicted than those of K_{dry} and V_P.

In the case of the Utsira Fm., although the mechanical models over predict the dry bulk modulus data, the fact that the zero friction model can explain the dry shear modulus and velocities data is consistent with the thinking that at shallower burial depths, and therefore lower effective stresses, the sediments and rocks are closer to the zero friction limit.

In the chemical compaction domain, the difference in values of dry bulk modulus for the same values of porosity (Figures 5.4 and 5.6) can be a result of different types of cement deposition (Figure 6.4.a)). In their study of two different groups of North Sea sandstones encountered at the same well, in the same porosity range, Dvorkin and Brevik (1999) interpreted the dry P-wave modulus (M_{dry}) differences as a result of the difference in the position of the quartz cement. They concluded that in the stiffer rocks the cement was located predominantly at the grain contacts, whereas in the "softer" rocks the cement was predominantly located away from these contacts.

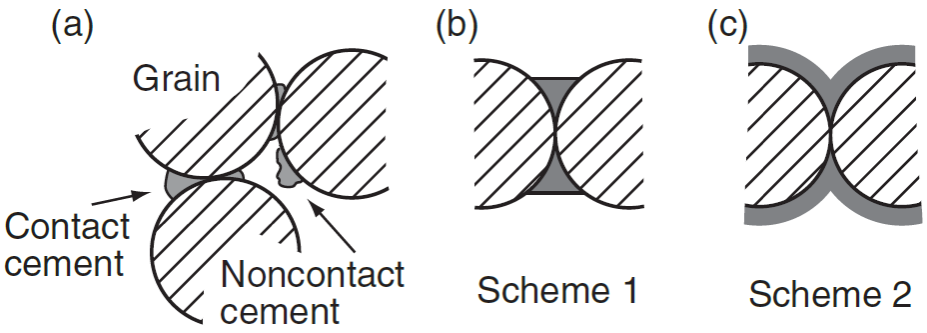

Figure 6.4. a) Schematic of types of cement deposition. b) All cement deposited at grain contacts. c) Cement deposited in uniform layer around grains. (From Mavko et al., 2009)

The chemical compaction models presented herein follow the scheme of cement deposited in uniform layers around grains for the contact-cement model (Figure 6.4.c)). The all cement deposited at grain contacts scheme (Figure 6.4.b)) results in higher values of elastic moduli, and therefore higher velocities (Dvorkin and Nur, 1996), indicating that the rock becomes stiffer by this type of cement deposition. This different scheme of quartz cement deposition might explain some of the great values of K_{dry} in Garn sandstones with about 0.25-0.30 porosity in comparison with lower values, at the same porosity, that follow the chemical compaction trend (Figure 5.6). However, this great difference in dry bulk modulus values is not observed for the dry shear modulus (Figure 5.7).

From the K_{dry} data versus porosity, it can also be observed that the values from the deeper and highly overpressured wells are usually the ones that are more over predicted by the model. Changes in the pressure regimes might also explain the variations in dry bulk modulus values at same porosities. In their study of velocity-depth trends in sediments from the Norwegian shelf, Storvoll et al. (2005) suggest that lower velocities in overpressured Jurassic sediments from Haltenbanken at 4-5 km burial depth (in comparison with equivalent hydrostatically pressured sequences) is a direct response to lower effective stresses and, therefore, reduced elastic compaction.

One of the main shortcomings of the Dvorkin-Nur contact-cement model is that it is not pressure sensitive (Avseth et al., 2010), however, in their application of the model to describe the Oseberg sandstones, they subjected the samples to different confining pressures and it can be observed that at lower confining pressures (< 30 MPa) the dry velocities from the samples fall below the theoretical model (Dvorkin and Nur, 1996).

In the case of dry shear modulus, the chemical compaction model greatly over predicts most of the values for the Etive and Garn formations, especially for the Etive Fm. In a previous study, Avseth et al. (2010) comment on the fact that the Dvorkin-Nur contact-cement model often over predicts shear stiffnesses in cemented sandstones. What is also to note from the data, is that the dry shear modulus values vary less at same values of porosity than the dry bulk modulus

values, which can be an indication of K_{dry} being more sensitive to the type of cement deposition, or to the pressure regime, than μ_{dry}.

The over prediction by the chemical compaction model in the 100% water saturated velocities, both for the Etive and Garn formations, follows from the over predictions in the K_{dry} (and subsequently, K_{sat}) and μ_{dry} models. The over predictions continue in the dry elastic moduli- and velocities-depth domain, especially at burial depths greater than 3.5 km, where the over predictions in the dry elastic moduli- and velocities-porosity domain combine with those from the porosity-depth domain.

Dvorkin and Nur (1996) rock physics diagnostics were initially presented to describe the velocity-porosity relationships in two different sets of samples, one made with slightly cemented quartz sands and the second one being almost completely uncemented, with two different models (the contact-cement model and the friable-sand model), and not to describe the continuous changes in the velocities (or elastic moduli) of sediments and rocks resulting from the diagenetic processes after deposition. This fact, together with the results presented in this study, enlighten the importance of well-defined models to describe and predict the changes in rock physical properties with burial depth, as a result of the mechanical and chemical compaction processes.

CHAPTER 7 CONCLUSIONS

In both the Etive Fm. and Garn Fm. the changes in physical properties with burial depth result from two different compaction processes: mechanical compaction and chemical compaction. These processes are greatly affected by rock microstructure, pressure regimes and temperature history

The mechanical compaction governs up to about 2 km burial depth, corresponding to temperatures around 75°C. The general under prediction of porosity values for the shallower sandstones (< 2 km burial depth) by the mechanical compaction model suggests that both Etive and Garn Fm. have high depositional porosities (> 0.40). On the other hand, the model's under prediction of dry bulk modulus and P-wave velocity in the same sandstones (at 1.6-2.0 km burial depth) suggests that these might be slightly cemented, with little amounts of quartz cement stiffening the rocks but not affecting their porosities significantly.

At burial depths greater than 2 km, chemical compaction is the main controlling process in the changes of physical properties. From temperature history curves, the Garn Fm. has slightly higher temperature increase rates than the Etive Fm., which is consistent with the porosity modeling in the chemical compaction domain. The greater variations in porosity values for the Garn sandstones at the same depth suggest that they are less well sorted than the Etive sandstones, and that the quartz cement also distributes less evenly. For both formations, there is a steep decrease in porosity from 2-3.5 km burial depth, and at greater depths there is, generally, no further significant reduction in porosity values (the porosities remain around 0.15-0.20). These high porosities at great burial depths (> 4 km) suggest the presence of significant amounts of clay coatings inhibiting the quartz cementation. The high overpressures reported in these sandstones indicate that the porosity preservation might also be influenced by low effective stresses.

In the dry bulk modulus-porosity domain, the greater variations in bulk modulus values for Garn sandstones with the same porosity suggests that they are more affected by different quartz deposition schemes than the Etive sandstones. For both formations, the values of dry bulk modulus for the highly overpressured sandstones are usually under predicted by the models.

From the general over predictions of dry elastic moduli and velocities at greater burial depths, it is recommended to use or develop models that take into account the effects of varying effective pressures in the chemical compaction domain.

BIBLIOGRAPHY

ARCHIE, G. E. 1952. Classification of carbonate reservoir rocks and petrophysical considerations. *AAPG Bulletin,* 36**,** 278-298.

AVSETH, P., MUKERJI, T., MAVKO, G. & DVORKIN, J. 2010. Rock-physics diagnostics of depositional texture, diagenetic alterations, and reservoir heterogeneity in high-porosity siliciclastic sediments and rocks—A review of selected models and suggested work flows. *Geophysics,* 75**,** 75A31-75A47.

BATZLE, M. & WANG, Z. 1992. Seismic properties of pore fluids. *Geophysics,* 57**,** 1396-1408.

BJØRLYKKE, K. & JAHREN, J. 2010. *Sandstones and sandstone reservoirs,* Springer.

BLYSTAD, P., BREKKE, H. & FAERSETH, R. B. 1995. *Structural Elements of the Norwegian Continental Shelf. Pt. 2. The Norwegian Sea Region,* Norwegian Petroleum Directorate.

BULLER, A., BJØRKUM, P., NADEAU, P. & WALDERHAUG, O. 2005. Distribution of Hydrocarbons in Sedimentary Basins. *Research & Technology Memoir***,** 15.

CHUHAN, F. A., KJELDSTAD, A., BJØRLYKKE, K. & HØEG, K. 2002. Porosity loss in sand by grain crushing—Experimental evidence and relevance to reservoir quality. *Marine and Petroleum Geology,* 19**,** 39-53.

DALLAND, A., WORSLEY, D. & OFSTAD, K. 1988. *A lithostratigraphic scheme for the mesozoic and cenozoic and succession offshore mid-and northern norway,* Oljedirektoratet.

DEEGAN, C. T. & SCULL, B. J. 1977. *A standard lithostratigraphic nomenclature for the Central and Northern North Sea,* HMSO.

DVORKIN, J. & BREVIK, I. 1999. Diagnosing high-porosity sandstones: Strength and permeability from porosity and velocity. *Geophysics,* 64**,** 795-799.

DVORKIN, J. & NUR, A. 1996. Elasticity of high-porosity sandstones: Theory for two North Sea data sets. *Geophysics,* 61**,** 1363-1370.

EHRENBERG, S. 1993. Preservation of anomalously high porosity in deeply buried sandstones by grain-coating chlorite: examples from the Norwegian continental shelf. *AAPG Bulletin,* 77**,** 1260-1286.

EHRENBERG, S. N. 1990. Relationship between diagenesis and reservoir quality in sandstones of the Garn Formation, Haltenbanken, mid-Norwegian continental shelf. *AAPG Bulletin,* 74**,** 1538-1558.

GELIUS, L. J. & WANG, Z. 2008. Modelling production caused changes in conductivity for a siliciclastic reservoir: A differential effective medium approach. *Geophysical Prospecting,* 56**,** 677-691.

GREENBERG, M. & CASTAGNA, J. 1992. Shear-wave velocity estimation in porous rocks: theoretical formulation, preliminary verification and applications. *Geophysical prospecting,* 40**,** 195-209.

HANSEN, S. 1996. Quantification of net uplift and erosion on the Norwegian Shelf south of 66 N from sonic transit times of shale. *Norsk Geologisk Tidsskrift,* 76**,** 245-252.

HANTSCHEL, T. & KAUERAUF, A. I. 2009. *Fundamentals of basin and petroleum systems modeling,* Springer Science & Business Media.

HELLAND-HANSEN, W., ASHTON, M., LØMO, L. & STEEL, R. 1992. Advance and retreat of the Brent delta: recent contributions to the depositional model. *Geological Society, London, Special Publications,* 61**,** 109-127.

LANDER, R. H. & WALDERHAUG, O. 1999. Predicting porosity through simulating sandstone compaction and quartz cementation. *AAPG bulletin,* 83**,** 433-449.

MARCUSSEN, Ø., MAAST, T. E., MONDOL, N. H., JAHREN, J. & BJØRLYKKE, K. 2010. Changes in physical properties of a reservoir sandstone as a function of burial depth – The Etive Formation, northern North Sea. *Marine and Petroleum Geology,* 27**,** 1725-1735.

MAVKO, G., CHAN, C. & MUKERJI, T. 1995. Fluid substitution: Estimating changes in Vp without knowing Vs. *Geophysics,* 60**,** 1750-1755.

MAVKO, G., MUKERJI, T. & DVORKIN, J. 2009. *The rock physics handbook: Tools for seismic analysis of porous media*, Cambridge university press.

NPD. 2016a. *Norwegian Petroleum Directorate FactMaps* [Online]. Available: http://gis.npd.no/factmaps/sl_21/ [Accessed 20.11.2016].

NPD. 2016b. *Norwegian Petroleum Directorate FactPages* [Online]. Available: http://factpages.npd.no/factpages/ [Accessed 01.09.2016].

NUR, A., MAVKO, G., DVORKIN, J. & GALMUDI, D. 1998. Critical porosity: A key to relating physical properties to porosity in rocks. *The Leading Edge,* 17**,** 357-362.

RAMM, M. 1992. Porosity-depth trends in reservoir sandstones: theoretical models related to Jurassic sandstones offshore Norway. *Marine and Petroleum Geology,* 9**,** 553-567.

STORVOLL, V., BJØRLYKKE, K., KARLSEN, D. & SAIGAL, G. 2002. Porosity preservation in reservoir sandstones due to grain-coating illite: a study of the Jurassic Garn Formation from the Kristin and Lavrans fields, offshore Mid-Norway. *Marine and Petroleum Geology,* 19**,** 767-781.

STORVOLL, V., BJØRLYKKE, K. & MONDOL, N. H. 2005. Velocity-depth trends in Mesozoic and Cenozoic sediments from the Norwegian Shelf. *AAPG Bulletin,* 89**,** 359-381.

THYBERG, B. & JAHREN, J. 2011. Quartz cementation in mudstones: sheet-like quartz cement from clay mineral reactions during burial. *Petroleum Geoscience,* 17**,** 53-63.

VOLLSET, J. & DORÉ, A. G. 1984. *A revised Triassic and Jurassic lithostratigraphic nomenclature for the Norwegian North Sea*, Oljedirektoratet.

WALDERHAUG, O. 1994a. Precipitation rates for quartz cement in sandstones determined by fluid-inclusion microthermometry and temperature-history modeling. *Journal of Sedimentary Research,* 64.

WALDERHAUG, O. 1994b. Temperatures of quartz cementation in Jurassic sandstones from the Norwegian continental shelf; evidence from fluid inclusions. *Journal of Sedimentary Research,* 64**,** 311-323.

WALDERHAUG, O. 1996. Kinetic modeling of quartz cementation and porosity loss in deeply buried sandstone reservoirs. *AAPG Bulletin,* 80**,** 731-745.

WALDERHAUG, O. 2000. Modeling quartz cementation and porosity in Middle Jurassic Brent Group sandstones of the Kvitebjørn field, northern North Sea. *AAPG bulletin,* 84**,** 1325-1339.

WALTON, K. 1987. The effective elastic moduli of a random packing of spheres. *Journal of the Mechanics and Physics of Solids,* 35**,** 213-226.

APPENDIX A

Tables A.1 and A.2 summarize the pore fluid properties in the intervals corresponding to the Etive Fm. and the Garn Fm. in the studied wells from the North Sea and the Norwegian Sea, respectively. The fluids densities and bulk moduli were calculated according to Batzle and Wang (1992) relationships (section 4.8). Gas gravities, oil API gravities, and gas-oil ratios were available from NPD's FactPages and completion reports. The average formation water resisitivities calculated in section 4.5 are also included.

Abbreviations used in the tables:

ρ_B	Brine density
K_B	Brine bulk modulus
ρ_G	Gas density
K_G	Gas bulk modulus
ρ_{Oil}	Oil density
K_{Oil}	Oil bulk modulus
G	Gas gravity
API	Oil API gravity
GOR	Gas-oil ratio
R_w	Formation water resistivity

Table A.1. Pore fluid properties in the Etive Fm. in the studied wells from the North Sea. When gas gravity or API gravity data were not available (N/A) values of 0.695 and 40 were used, respectively.
* Dry well
** Wells with both gas and oil content in the Etive Fm. (see GOR) resulting in low oil densities and bulk moduli.
*** Wells with oil shows, GOR set to 20 m^3/m^3.

Well	ρ_B (g/cm^3)	K_B (GPa)	ρ_G (g/cm^3)	K_G (GPa)	ρ_{Oil} (g/cm^3)	K_{Oil} (GPa)	G	API	GOR (m^3/m^3)	R_w (Ω.m)
34/10-9	1.0162	2.6392	-	-	0.7949	1.1086	N/A	31.9	62	0.1066
34/10-3	1.0173	2.6935	-	-	0.7926	1.0341	0.656	29.2	70	0.0794
34/7-12	1.0037	2.6496	-	-	0.7481	0.8561	0.722	36.8	68	0.0861
30/6-10**	1.0127	2.6967	-	-	0.3100	0.0849	0.673	47.2	1595	0.0959
30/3-4	0.9693	2.4536	-	-	0.6945	0.5539	0.770	38.0	80	0.0564
34/10-17	0.9940	2.6414	-	-	0.6117	0.3848	0.740	35.0	246	0.0721
34/10-2**	0.9786	2.5194	-	-	0.2314	0.6926	0.645	43.0	3800	0.0507
33/12-7*	0.9897	2.6288	-	-	-	-	-	-	-	0.0657
30/6-11***	0.9853	2.6098	-	-	0.7483	0.9259	N/A	N/A	N/A	0.0647
34/8-6***	0.9874	2.6368	-	-	0.7859	1.0753	N/A	N/A	N/A	0.0619
34/10-21	0.9944	2.6741	0.2043	0.0828	-	-	0.650	-	-	0.0609
30/2-2	0.9628	2.4492	0.2262	0.0977	-	-	0.734	-	-	0.0533
34/10-23	0.9626	2.4549	0.2045	0.0974	-	-	0.650	-	-	0.0549
34/11-4	0.9596	2.4289	0.2182	0.1005	-	-	N/A	-	-	0.0630
34/8-7	0.9540	2.3940	0.2268	0.1109	-	-	0.695	-	-	0.0500

Table A.2. Pore fluid properties in the Garn Fm. in the studied wells from the Norwegian Sea. When gas gravity or API gravity data were not available (N/A) values of 0.695 and 40 were used, respectively. Note that most of the wells containing oil have higher gas-oil ratios than those in the North Sea, resulting in lower oil densities.
* Dry wells
** Well with both gas and oil content in the Garn Fm. where GOR was not available, and set to 700 m^3/m^3.
*** Well with oil shows, GOR set to 20 m^3/m^3.

Well	ρ_B (g/cm^3)	K_B (GPa)	ρ_G (g/cm^3)	K_G (GPa)	ρ_{Oil} (g/cm^3)	K_{Oil} (GPa)	G	API	GOR (m^3/m^3)	R_w (Ω.m)
6507/12-3*	1.0119	2.6561	-	-	-	-	-	-	-	0.0982
6507/8-6*	0.9946	2.6637	-	-	-	-	-	-	-	0.0944
6507/11-3	1.0069	2.6766	0.1783	0.0539	-	-	0.670	-	-	0.0801
6608/10-2	0.9803	2.5249	0.1532	0.0550	-	-	0.645	-	-	0.0709
6507/8-7*	0.9946	2.6394	-	-	-	-	-	-	-	0.0663
6507/11-6	0.9949	2.6535	0.2026	0.0717	-	-	N/A	-	-	0.0678
6507/5-1	0.9725	2.5039	-	-	0.2167	1.1381	0.670	54.9	4164	0.0613
6507/2-2	0.9728	2.5183	0.1864	0.0828	-	-	0.630	-	-	0.0556
6407/1-3	0.9821	2.5920	-	-	0.2315	0.8058	0.655	50.8	3458	0.0594
6406/3-6**	0.9713	2.5071	-	-	0.4091	0.2226	N/A	N/A	N/A	0.0546
6506/12-3	0.9693	2.4972	-	-	0.5054	0.2847	0.781	40.0	408	0.0557
6506/12-6	0.9639	2.4657	0.2432	0.1063	-	-	0.765	-	-	0.0519
6406/6-1***	0.9552	2.3890	-	-	0.7030	0.7328	N/A	N/A	N/A	0.0510
6406/2-7	0.9524	2.3753	-	-	0.4041	0.3702	N/A	44.1	731	0.0492
6406/2-3	0.9496	2.3536	-	-	0.3953	0.4025	0.720	47.2	744	0.0475

APPENDIX B

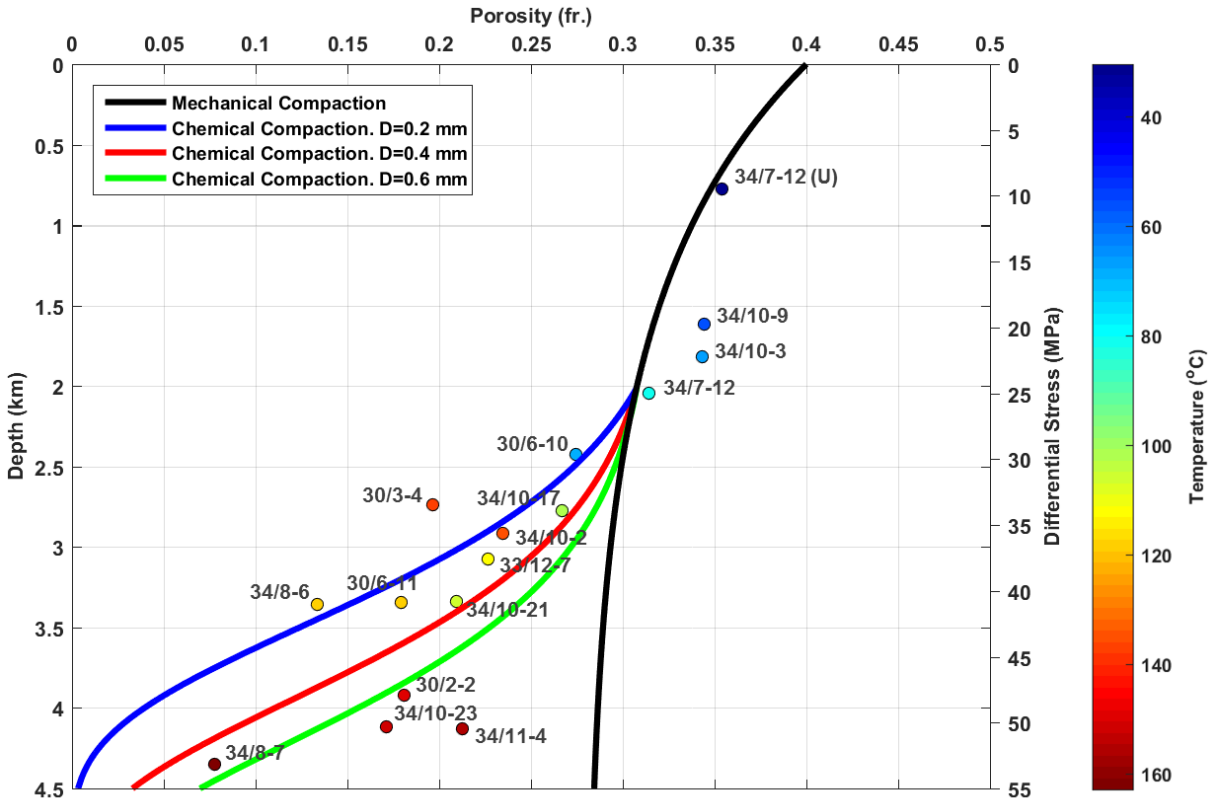

Figure B.1. Porosity-depth trends in the mechanical and chemical domains for the sandstones of the Etive Fm. color-coded by Formation temperature. The porosity values correspond to the median porosity value for each well. Well names are indicated. U = Utsira Fm., *D* = grain size.

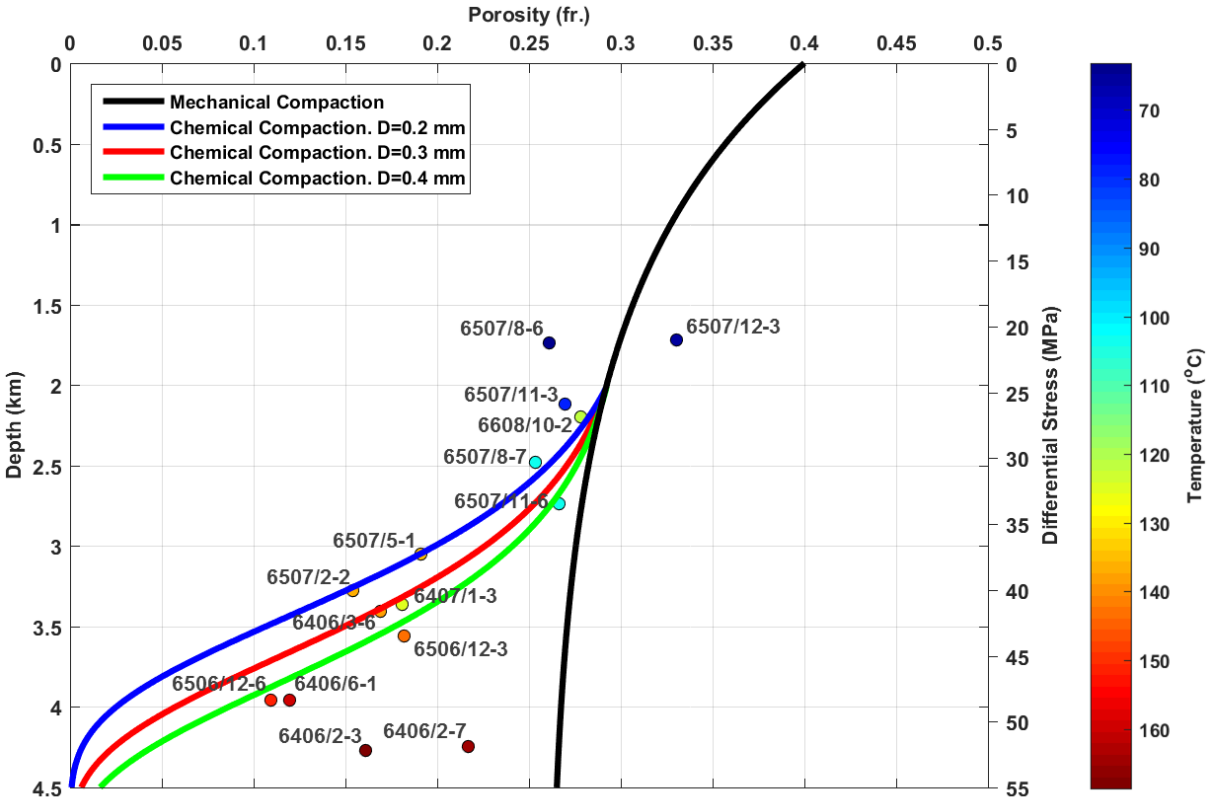

Figure B.2. Porosity-depth trends in the mechanical and chemical domains for the sandstones of the Garn Fm. color-coded by Formation temperature. The porosity values correspond to the median porosity value for each well. Well names are indicated. *D* = grain size.

APPENDIX C

The median values of porosity, bulk density at 100% water saturation, dry stiffness moduli, and wave propagation velocities at 100% water saturation versus burial depth are presented for the Etive Fm. and the Garn Fm. (the values from the Utsira Fm. are not included). For each of these properties, the data from the Etive and Garn sandstones are presented together.

For each Formation, linear regressions are included for every property. Note how the linear regressions result in unphysical values at zero burial depth.

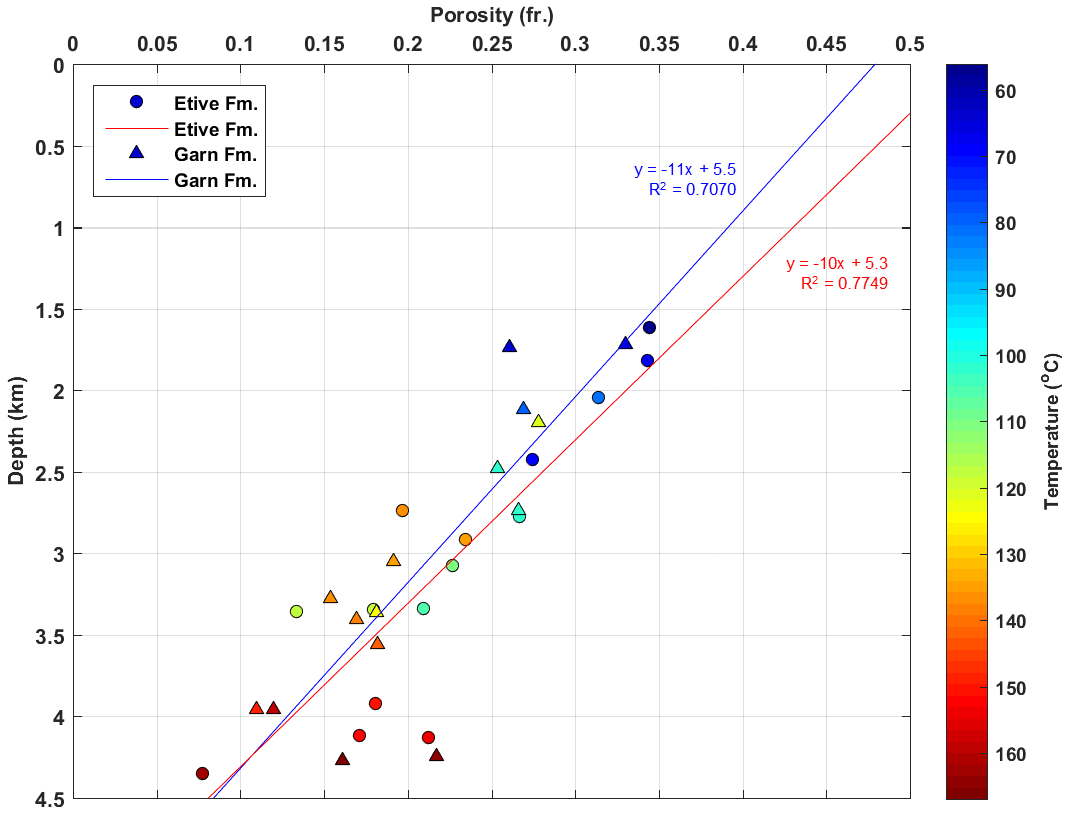

Figure C.1. Median values of porosity versus burial depth for the Etive Fm. and the Garn Fm. Linear regressions for the data from each Formation are included.

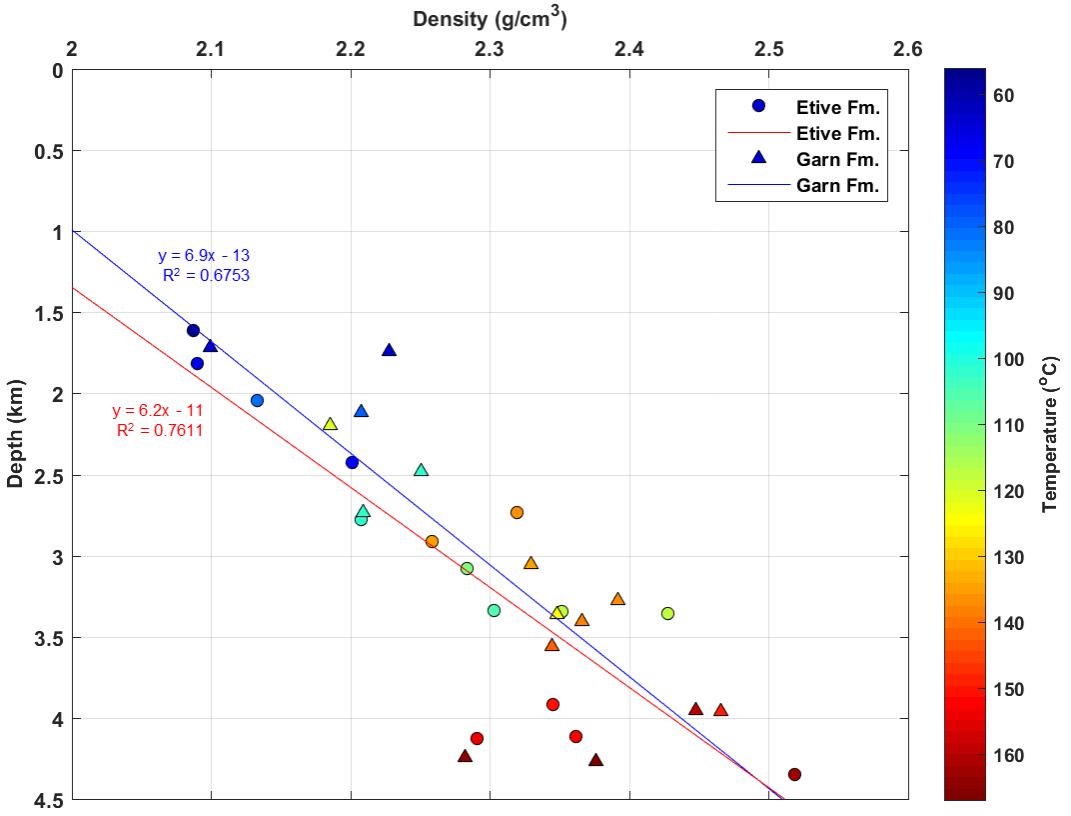

Figure C.2. Median values of bulk density (S_w=100%) versus burial depth for the Etive Fm. and the Garn Fm. Linear regressions for the data from each Formation are included.

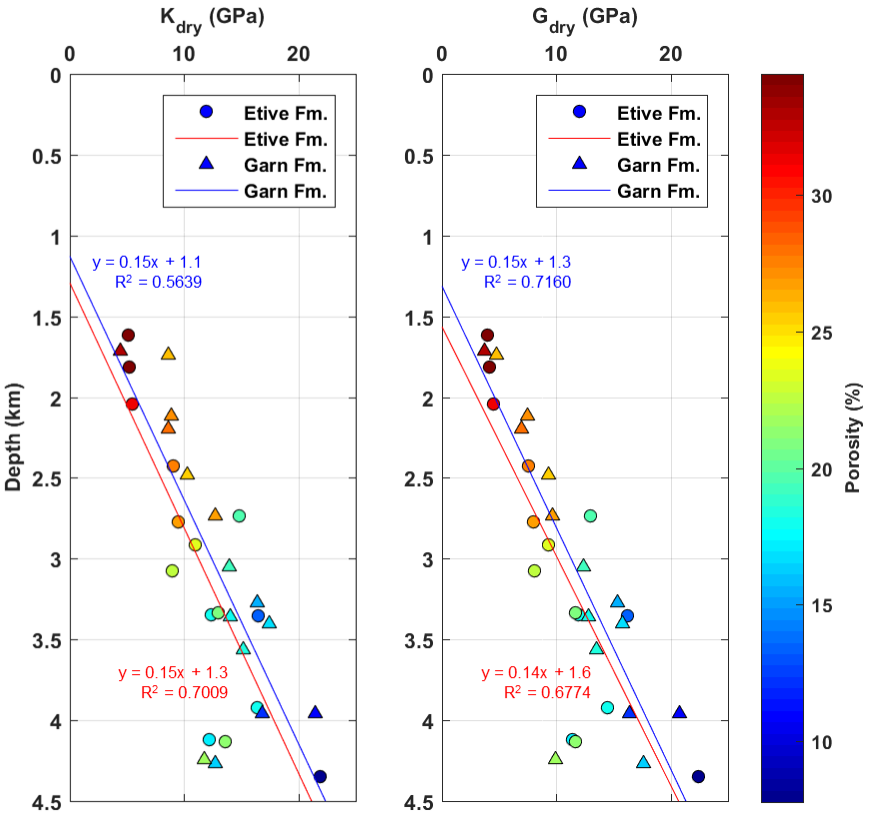

Figure C.3. Median values of dry elastic moduli versus burial depth for the Etive Fm. and the Garn Fm. Linear regressions for the data from each Formation are included.

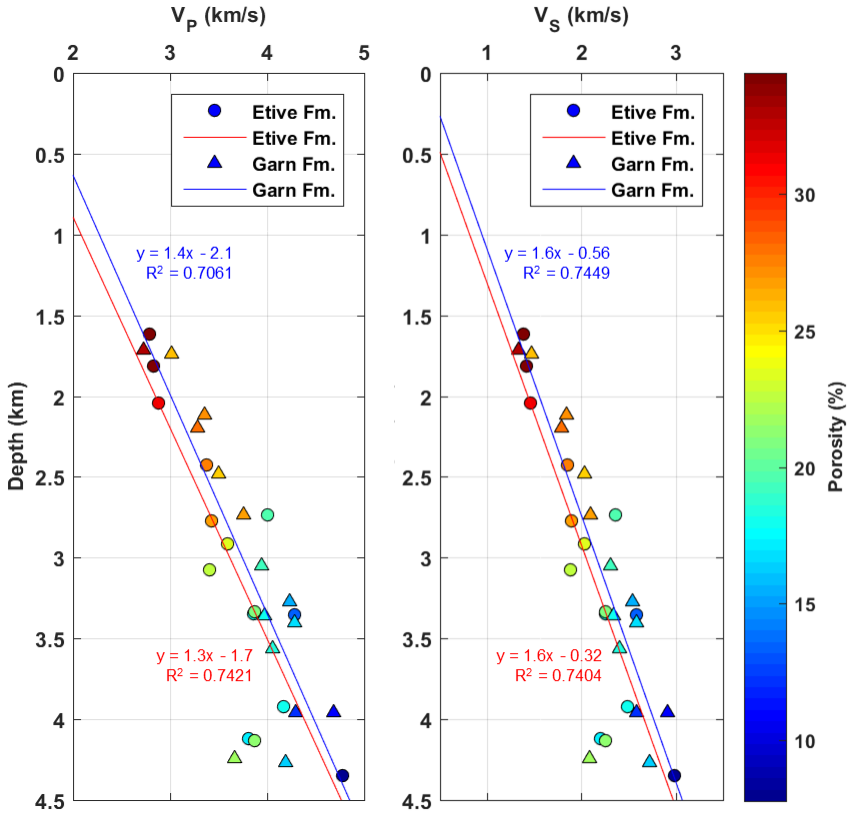

Figure C.4. Median values of wave propagation velocities (S_w=100%) versus burial depth for the Etive Fm. and the Garn Fm. Linear regressions for the data from each Formation are included.